Title

SUMOylation Inhibition as a Strategy to Inhibit Pancreatic Cancer Liver Metastasis

Author

Ren, Tianchen

Publication Date

2023

UNIVERSITY OF CALIFORNIA SAN DIEGO

SUMOylation Inhibition as a Strategy to Inhibit Pancreatic Cancer Liver Metastasis

A Thesis submitted in partial satisfaction of the requirements
for the degree Master of Science

in

Chemistry

by

Tianchen Ren

Committee in charge:

Professor Yuan Chen, Chair
Professor Patricia Jennings, Co-Chair
Professor Jin Zhang

2023

The Thesis of Tianchen Ren is approved, and it is acceptable in quality and form for publication on microfilm and electronically.

University of California San Diego

2023

DEDICATION

This thesis is dedicated to my beloved family for their unwavering support and boundless love. Their encouragement, understanding, and sacrifices have fueled and guided me through the challenges. To my mentors, friends, and all those who have played a role in shaping my academic path.

TABLE OF CONTENTS

LIST OF FIGURES

LIST OF TABLES

LIST OF ABBREVIATIONS

AdoS	Adenosine sulfamate
ALDH	Aldehyde dehydrogenase
AMP	Adenosine monophosphate
ATP	Adenosine triphosphate
BKG	Background
CCL	C-C motif Chemokine Ligand
CD	Clusters of differentiation
Col	Collagen
CSCs	Cancer stem cells
DMEM	Dulbecco's Modified Eagle Medium
DMSO	Dimethyl Sulfoxide
E1	Enzyme 1
E2	Enzyme 2
E3	Enzyme 3
Env	Envelope protein
FLuc	Firefly Luciferase
Gag	Group Antigens
HIV	Human immunodeficiency virus
H&E	Hematoxylin and eosin stain
IC50	Inhibitory Concentration 50
IL	Interleukin
IP	Intraperitoneal

IRES	Internal Ribosome Entry Sites
KPC	Kras, p53, and Cre
LC-MS	Liquid chromatography-mass spectrometry
Luc	Luciferase
NK	Natural Killer
NMR	Nuclear Magnetic Resonance
PAGE	Polyacrylamide gel electrophoresis
PBMC	Peripheral blood mononuclear cells
PBS	Phosphate-buffered saline
PDAC	Pancreatic ductal adenocarcinoma
Pol	Polymerase
PPi	Pyrophosphates
REV	Regulator of expression of virion proteins
ROI	Region of interest
RRE	Rev response element
RSV	Respiratory syncytial virus
SAE	Small Ubiquitin-like Modifier Activating Enzyme
SDS	Sodium Dodecyl Sulfate
SUMO	Small Ubiquitin-like Modifier
Tcm	Central memory T cells
Tem	Effector memory T cells
Tgf-β	Transforming growth factor-β
Tn	Naive T cells

UBC9	Ubiquitin carrier protein 9
UBL	Ubiquitin-Like
VC	Vehicle control
Veh	Vehicle
VSV-G	Vesicular stomatitis virus G

ACKNOWLEDGEMENTS

I would like to acknowledge all the individuals in Chen Lab for their invaluable contributions to this research. Your guidance, support, and advice have been instrumental in shaping the outcomes of this thesis. I also want to express my gratitude to Lowy's Lab for their support and insightful contributions in enriching the depth of this work. To both labs, I would like to thank everyone for fostering an environment of collaboration and shared knowledge.

ABSTRACT OF THE THESIS

SUMOylation Inhibition as a Strategy to Inhibit Pancreatic Cancer Liver Metastasis

by

Tianchen Ren

Master of Science in Chemistry

University of California San Diego, 2023

Professor Yuan Chen, Chair
Professor Patricia Jennings, Co-Chair

Pancreatic ductal adenocarcinoma (PDAC) is the 3rd leading cause of cancer-related death in the United States. PDAC is highly metastatic with the liver being the most common site of metastasis. Notably, even after surgical resection of early stage of PDAC tumors, recurrence often occurs in the liver instead of the primary site that was surgically treated, suggesting the existence of micrometastasis in the liver of early-stage diseases. There is currently no approach to treat or prevent liver metastasis besides chemotherapy that is highly toxic and lacks efficacy. Therefore, new therapeutic targets need to be investigated to make a difference in patients' outcomes. My thesis research project is to investigate small ubiquitin-like modification (SUMOylation) as a target to prevent and treat PDAC liver metastasis. SUMOylation is a reversible post-translational modification involving the attachment of a SUMO protein covalently to a target protein. Previous studies have shown that SUMOylation is required for KRas and c-Myc-dependent oncogenesis that are main drivers of PDAC progression. In addition, SUMOylation has been established as a target for activation of anti-tumor immunity. My findings suggest that SUMOylation inhibition can block PDAC liver metastasis. The mechanisms could be through both immune-mediated and tumor-specific effects.

CHAPTER 1: BACKGROUND AND INTRODUCTION

1-1 PDAC and Liver Metastasis

Pancreatic ductal adenocarcinoma (PDAC) is a highly malignant cancer, ranking as the third leading cause of cancer-related mortality in the United States, with an alarming 12% overall survival rate at 5 years (*1*). Its poor prognosis is exacerbated by diagnostic challenges and the limited efficacy of standard of care, including chemotherapy and radiation therapy (*2*). PDAC manifests as a systemic disease upon diagnosis, often spreading to various organs, with a notable preference for the liver. Even after surgical resection, the liver remains a common site for recurrence .

Metastasis, a leading cause of PDAC mortality, involves the detachment of neoplastic cells from the primary tumor, transit through blood and lymph vessels, and the subsequent establishment of metastasized tumors at distant sites (*3*). Importantly, these metastatic tumors maintain the histological characteristics of the primary tumor (*3*). Understanding the molecular mechanisms governing metastasis is pivotal for advancing targeted interventions and improving outcomes in metastatic cancers.

1-2 SUMOylation and its corresponding effects

SUMOylation is a reversible post-translational modification that alters the regulation of protein functions. SUMOylation was previously found as required for KRas and c-Myc-dependent oncogenesis that are major oncogenic drivers for PDAC progression through regulating cellular processes including transcription, subcellular localization, and mitosis (*4*). Oncogenesis driven by the Ras pathway and its downstream effectors requires SUMOylation, a process modulating their activities and localization with significance in sustaining the transformation growth of KRAS mutant cancers (*5*). The formation of a feed-forward loop between SUMOylation and c-Myc adds another layer of complexity to the regulation of cellular processes, in terms of oncogenesis (*4*, *6*). Studies have proved that inhibiting SUMOylation has therapeutic benefits for Myc driven cancer (*7*). In addition, SUMOylation in immune cells is recently found to function as a central repressor of the expression of type I interferon (IFN) (*8*, *9*). Thus, inhibition of SUMOylation is a new immuno-oncology approach currently evaluated in Phase 2 clinical trials of multiple solid tumors. Unfortunately, PDAC is not included in these clinical trials due to lack of preclinical data. Thus, my thesis research is timely in exploring whether SUMOylation can be targeted to prevent and treat PDAC liver metastasis.

In murine cells, SUMO proteins consist of three paralogs, SUMO-1, SUMO-2, and SUMO-3 while mammalian cells consist of four paralogs, SUMO-1 to -4. SUMO-2 and SUMO-3 share 96% sequence identity and only differ by three N-terminal residues (*10*). They show about 50% sequence identity with SUMO-1. All SUMO proteins share a similar three-dimensional structure with ubiquitin. SUMO-4, expressed in the immune cells, on the other hand, is the least understood among the SUMO isoforms (*11*). The immune cell-specific expression of human SUMO-4 underscores the importance of SUMOylation in immune response.

1-3 SUMOylation enzymatic activity cascades

SUMOylation is a reversible post-translational modification of the intracellular protein. The enzymatic cascades include activation, conjugation, and ligation (*9*). The activation of the mature SUMO protein is facilitated by the heterodimeric SUMO-activating enzyme (SAE, a E1) (SAE1/SAE2) forming an acyl-adenylate intermediate (*9*). This ATP-dependent reaction leads to the formation of a thioester bond between the carboxyl glycine residue of SUMO protein and a cysteine residue in the E1 enzyme.[3] The activated SUMO protein is transferred to the active site cysteine of the E2 conjugating enzyme, Ubc9, through thioester exchange (*12*). Subsequently, a SUMO protein is transferred to the lysine residue to the target protein, leading to the formation of oligomers via isopeptide bonds that is often catalyzed by an E3 (*9*, *12*) SUMOylated target proteins can undergo desumoylation catalyzed by SUMO-specific proteases which release an unmodified target protein and a mature SUMO protein again (*12*). This allows fast enzymatic control of SUMO conjugation and deconjugation.

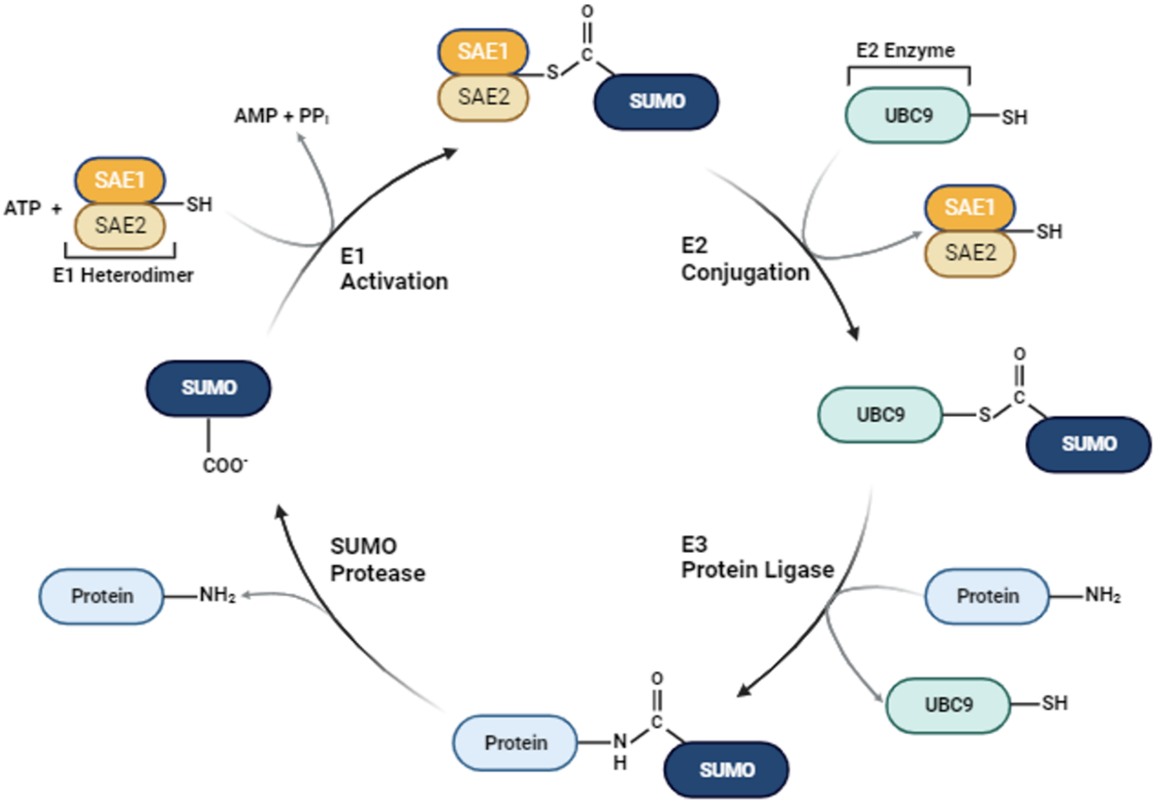

Figure 1. Enzymatic cascade of SUMOylation (Created with BioRender.com).

1-4 SUMOylation inhibition mechanism

Adenosine sulfamate (AdoS) has been found previously to derive the inhibition of E1 enzymes of ubiquitin-like (Ubl) modifications through mechanism-based inhibition (*13*, *14*). The sulfamate nucleophilically attacks the thioester intermediate through the reaction of sulfamate moiety with a cysteine thioester found in the E1 and a Ubl resulting in a covalent adduct-formation (*9*). This Ubl-AdoS adduct effectively binds and inhibits the respective Ubl E1 enzyme (*9*).

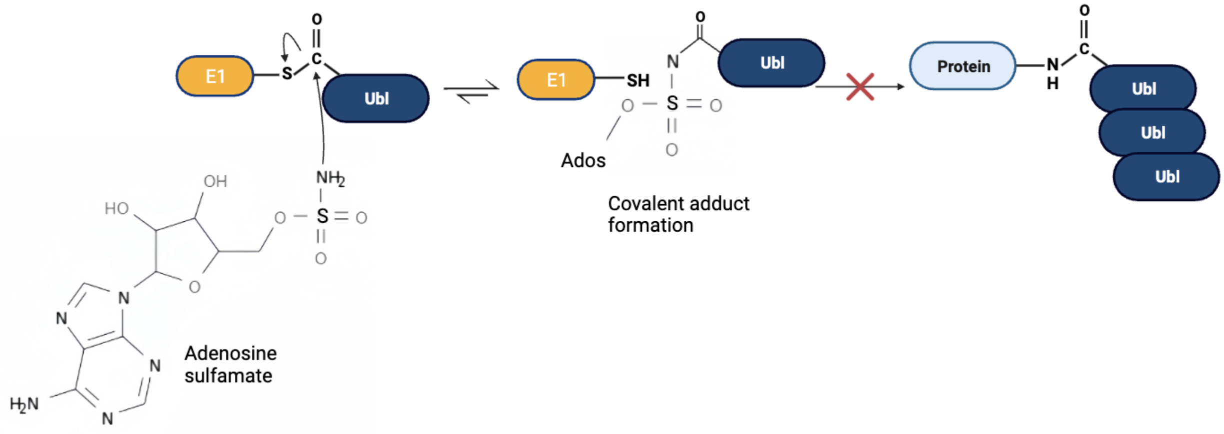

Figure 2. Mechanism of Inhibition of Ubl E1 enzyme by Adenosine Sulfamate Analogues (Created with BioRender.com).

TAK-981 designed by Takeda Pharmaceuticals is a mechanism-based inhibitor of SAE which forms a SUMO–TAK-981 adduct catalyzed by the target. They discovered an Adenosine analog with a Cyclopentyl Ring, Pyrimidine, and Tetrahydroisoquinoline on Thiophene (Fig. 3). Unlike an AdoS, TAK-981 targets the SAE-SUMO thioester intermediates to form a adduct with a SUMO protein with high specificity, with ~1000 fold selectivity over homologous enzymes (*9*, *15*).

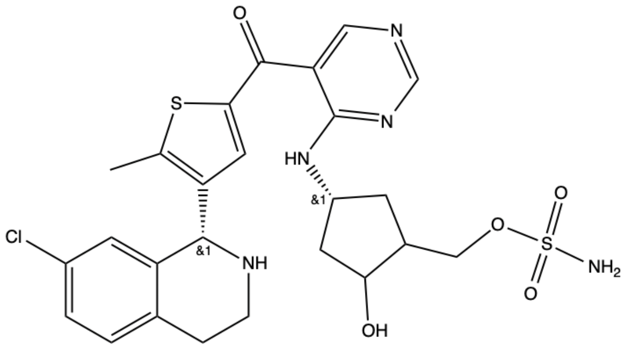

Figure 3. TAK-981 chemical structure.

1-5 SUMOylation in PDAC

In numerous cancer types, there is an upregulation of SUMOylation (*16*). A comparison of the expression profiles between PDAC tumors and adjacent non-tumor tissue samples demonstrated increased expression of key SUMO pathway components, such as SAE1, UBA2, UBE2I, SUMO1, SUMO2, and SUMO3 in PDAC (*16*). Survival analysis of pancreatic cancer patients, considering the expression of SUMOylation cascades related proteins, SAE1 (*17*), SUMO1 (*18*), SUMO2 (*19*), SUMO3 (*20*), UBA2 (*21*), UBE2I (*22*) reveals that higher expression is associated with a worse survival rate (Fig. 4). Thus, analysis of data from patient tissues supports that SUMOylation is a potential target to treat PDAC and that inhibiting SUMOylation could potentially lead to an improved survival rate in PDAC cancer.

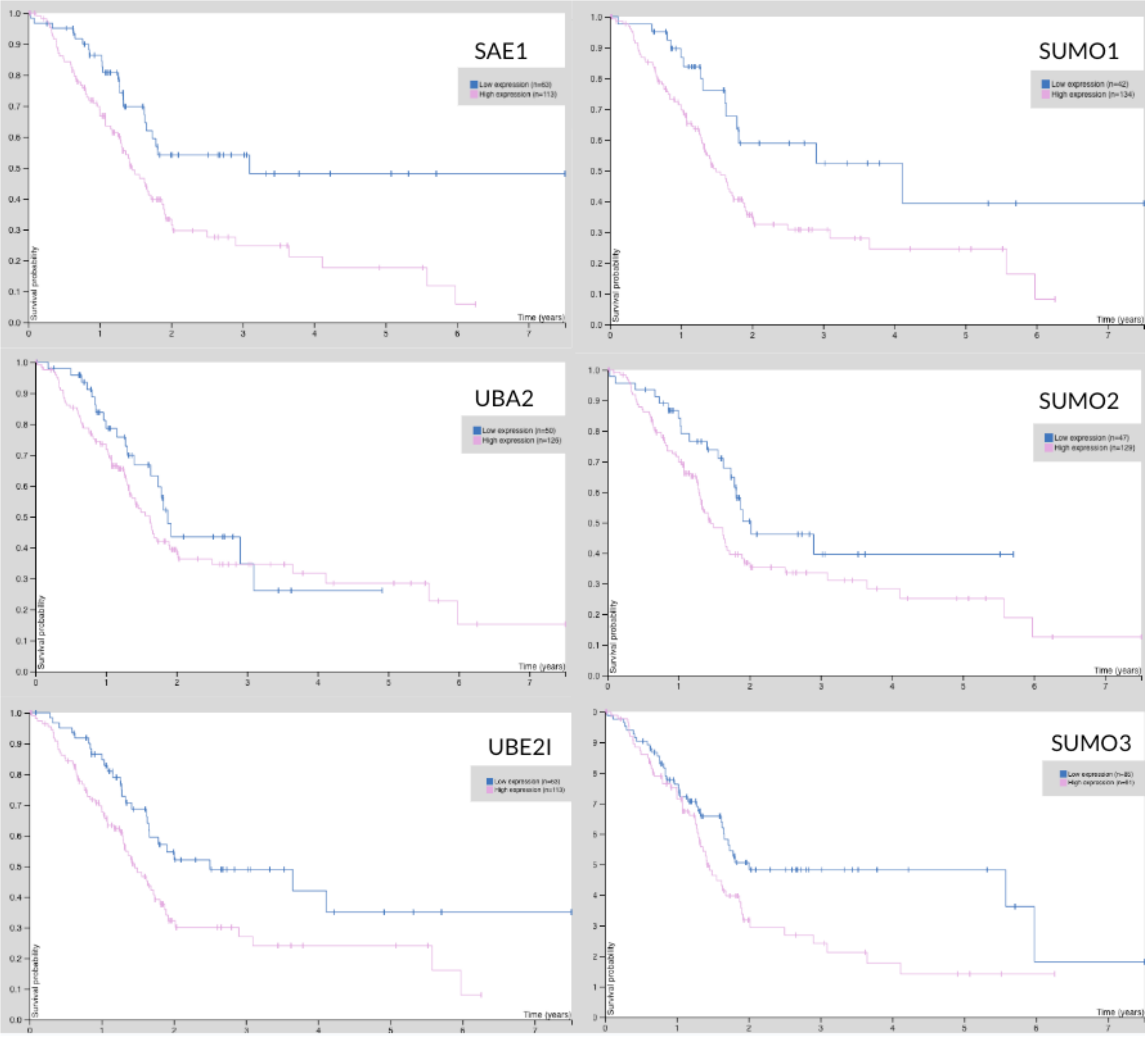

Figure 4. Survival analysis of PDAC patients with SAE1, UBA2; UBE2I, and SUMO1/2/3 expression level from Human protein atlas. (Blue: low expression; Pink: high expression) Dead (n = 92), Alive (n = 84); SAE1: p-value = 0.0019; UBA2: p-value = 0.26; UBE2I: p-value = 0.0076; SUMO1: p-value = 0.0071; SUMO2: p-value = 0.051 ; SUMO3: p-value = 0.021.

1-6 PDAC Liver Metastasis orthotopic *in vivo* mouse model

A well-established model of PDAC liver metastasis is by inducing liver metastases through intrasplenic injection of tumor cells. The spleen and liver are anatomically connected through the portal vein. Blood exits the spleen via the splenic vein, which then converges into the portal vein—a larger vessel responsible for transporting blood to the liver (*23*, *24*). The intrasplenic injection model induces tumor formation specifically in the liver. This model allows us to investigate the molecular mechanism of SUMOylation inhibition and its potential effects on preventing liver metastasis (*25*).

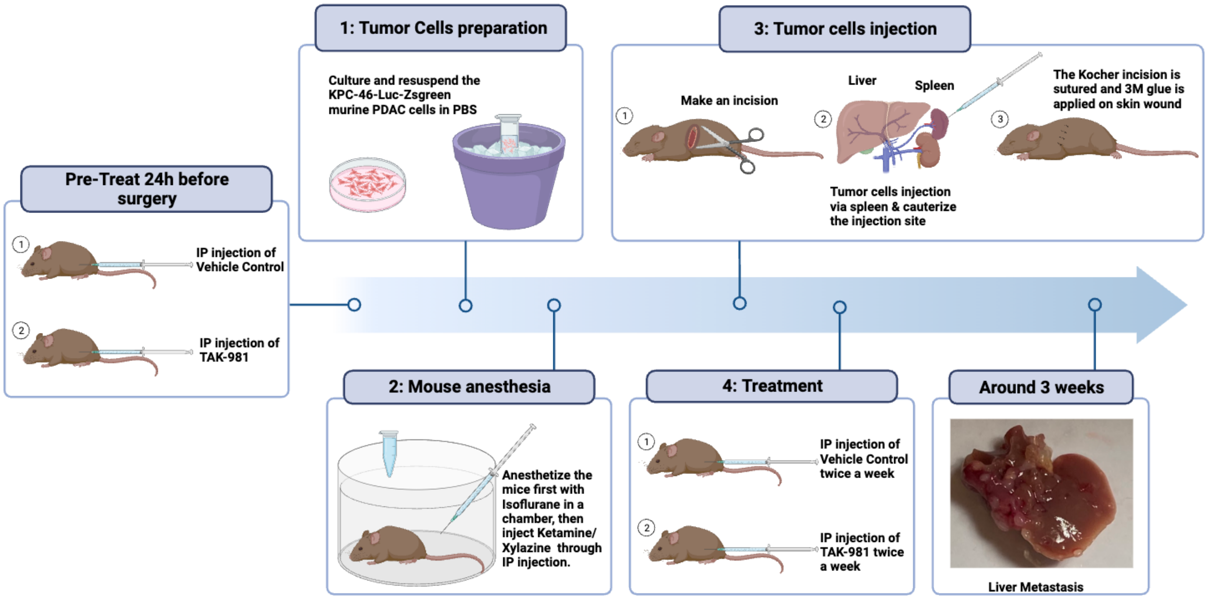

Figure 5. Orthotopic murine intrasplenic injection scheme (Created with BioRender.com).

KPC, representing Kras, p53, and Cre. Kras and p53 are frequently mutated genes in human pancreatic tumors. Cre functions as a specialized tool gene, regulating the activation of Kras and p53 in specific locations. KPC-46 was developed from liver metastasis of a male *Kras*$^{LSL\text{-}G12D}$*-p53*$^{LSL\text{-}R172H}$*-Pdx-1-Cre (KPC)* mouse bearing pancreatic carcinoma in Dr. Andrew Lowy's Lab at Moores Cancer Center. The KPC-46 cell line was employed to establish liver metastasis of PDAC. The use of mouse tumor cell line allows us to establish the tumor model in fully immune competent mice to examine both immune-mediated responses and tumor-specific effects.

1-7 The central hypothesis

Upregulation of SUMOylation has been observed in PDAC patients. I hypothesize that inhibiting SUMOylation is a novel strategy to block PDAC liver metastasis through multifaceted mechanisms, including suppressing the formation of metastatic niche, activating anti-tumor immune responses, and inhibiting tumor cells.

CHAPTER 2: METHODOLOGIES

2-1 TAK-981 stock solution preparation

100 mg TAK-981 powder was purchased from Chemitek (CT-TAK981) and resuspended in 833.4 µl pharmaceutical 99.9% purity DMSO (Millipore Sigma, RTC000103) to a stock concentration of 120 mg/ml. For long-term storage, the stock solution of TAK-981 was aliquoted and stored at -20°C.

2-2 Liquid chromatography-mass spectrometry

The stock solution of TAK-981 from Takeda Pharmaceuticals at 120 mg/ml was diluted to 1 mg/ml in pharmaceutical 99.9% purity DMSO (Millipore Sigma, RTC000103) in 50 µl and was set as a standard control. The stock solution of commercial TAK-981 from Chemitek at 120mg/ml was also diluted to 1mg/ml in pharmaceutical 99.9% purity DMSO in 50uL. Both samples were analyzed using LC-UV-ESI-MS (Thermo LCQdeca, ESI, HP 1100 LC station) at UC San Diego biochemistry MOLECULAR MASS SPECTROMETRY Core The flow rate: 1.000 ml/min; stop time: 20min; 95% solvent A: H_2O w/ 0.1% Formic Acid; 5% solvent B: Acetonitrile w/ 0.1% Formic Acid; pressure limits 450 bar max.

2-3 Nuclear Magnetic Resonance (NMR) spectroscopy

Stock solution of commercial TAK-981 from Chemitek at 120 mg/ml was also diluted to 1 mg/mL Deuterated water. The sample was analyzed at UC San Diego Skaggs School of Pharmacy and Pharmaceutical Sciences NMR facility (600 MHz Brucker). The DMSO percentage contained in the stock solution was calculated as below: The stock solution is made by resuspending 100 mg of TAK powder in 833. 4 µl of DMSO

Mass of DMSO in the stock solution = 1.1 $\frac{g}{ml}$ × 0. 8334 ml = 0.91674 g

120 mg/ml TAK solution = 207.6 mM TAK solution

To make 500 µl 1mM TAK solution in D_2O, we need 2.40 µl of 120 mg/ml stock solution diluted with 497.6 µl of D_2O.

The volume of stock TAK needed = $\frac{500\ \mu l\ final\ volume \times\ 1mM\ TAK\ in\ D2O}{207.6\ mM}$ = 2.408477842 µl

Volume of D_2O needed to make 1mM = 500 µl - 2.408477842 µl = 497.5915222 µl

Mass of DMSO in 2.40 µl stock solution for making 1mM TAK solution = $\frac{2.40\ \mu l}{833.4\ \mu l}$ × 0.91674 g = 0.002649325626 g

g/l TAK in 1 mM = 1 mM × 668.14 $\frac{g}{mol}$ = 1 $\frac{mol}{L}$ × 668.14 $\frac{g}{mol}$ = 0.66814 $\frac{g}{L}$

Mass of 1mM TAK solution in 1mL = 0.66814 $\frac{g}{L}$ × 0.0005 L = 0.00033407 g

Mass of D_2O in 500 µl of 1 mM TAK = 497.5915222 µl × 1.11 $\frac{g}{ml}$ = 0.5523265896 g

The total mass of DMSO + TAK + D_2O in the 500 µl of 1mM TAK in D_2O = 0.002649325626 g + 0.00033407 g + 0.5523265896 g = 0.5555506018 g

w/w % of DMSO in 1mM TAK solution = $\frac{0.002649325626\ g}{0.5555506018\ g}$ × 100 = 0.5201942371 %

Therefore, the DMSO NMR signal should not interfere with NMR data acquisition, because the concentration would be similar to that of TAK-981.

2-4 KPC Cell Culture

The mouse PDAC cell line, KPC-46 (obtained from Dr. Lowy's lab at Moores Cancer Center), was cultured in DMEM, high glucose, GlutaMAX™ Supplement, pyruvate (Gibco). Media were supplemented with 10% heat-inactivated fetal bovine serum (Corning) and 1%

Antibiotic-Antimycotic(Gibco). These cells were cultured in an incubator at 37 °C in humidified air with 5% CO_2.

2-5 RNA isolation, cDNA synthesis, and qPCR analysis

Hepatic stellate cells (HSCs) were collected in Trizol. ¼ of Chloroform was added to Trizol and thoroughly mixed by vortexing, then incubated on ice for 10 minutes. The mixture was spun down in a pre-cold 4°C centrifuge at 12,000rpm, for 10 minutes. The mixture was separated into three layers and the colorless upper aqueous phase containing RNA was collected. The same volume of isopropanol was added to the RNA and spun down at 12,000 rpm, 10 minutes, 4°C. The supernatant was discarded, and the pellet was resuspended in 200 µl 75% ethanol to wash out DNA and spun down at 12,000 rpm, 10 minutes, 4°C. The supernatant was regarded, and the pellet was left at room temperature for 5 minutes to evaporate the ethanol. 20µL of RNase-free water was added and waited for 30 minutes to dissolve the pellet. The final RNA concentration was measured using NanoDrop One^{c} (Thermoscientific). And optimal OD_{260}/OD_{280} is observed between 1.8 - 2.2.

cDNA was synthesized from the RNA using PrimeScript RT Reagent Kit with gDNA Eraser (Perfect Real Time) (Takara). 2 µg of RNA was calculated. For the Genomic DNA elimination reaction, 2.0 µl of 5X gDNA Eraser Buffer, 1.0 µl gDNA Eraser, RNA, and RNase Free dH_2O were mixed to a final volume of 10µl. The mixture was placed in the thermocycler (Bio-Rad) at 42 °C for 2 min. For reverse-transcription reaction, the mixture from the first step was placed on ice and mixed with 4.0 µl 5X PrimeScript Buffer 2 (for Real Time), 1.0 µl PrimeScript RT Enzyme Mix I Master mix, 1.0 µl RT Primer Mix^{*4} and 4.0 µl RNase Free dH_2O

to a final volume of 20 µl. The mixture was placed in the thermocycler (Bio-Rad) at 37°C for 30 min, 85°C for 5 sec, and kept at 4°C.

For q-PCR analysis, 0.25 µl of each forward and reverse primer of 18s, TGF-β, Ccl20, IL1a, IL6, 18S were used (provided by Dr. Andrew Lowy's Lab). 5 µl of PowerUp™ SYBR™ Green Master Mix (applied biosystems) and 2.5 µl of RNase Free dH_2O were mixed to a final volume of 10 µl. 8 µl of the mixture were loaded separately into the 384-well plate (applied biosystems) and 2 µl of cDNA was added after. The plate was shaken, spun down, and measured in QuantStudio5 (applied biosystems).

2-6 Cell proliferation assay

KPC-46 cells were seeded in two black 96 well plates (Thermo Sci.). Different concentrations calculated from 1 M TAK-981 and the following concentrations, 10 nM, 70 nM, 100 nM, 200 nM, 500 nM, 800 nM, 1000 nM, 1600 nM of TAK-981 were added on day 2. At day 3 (24h after TAK-981 treatment), media was replaced with fresh DMEM complete media for another 24 hours. On day 4, the cells were lysed with lysis buffer (Promega) in one plate to generate a luminescent signal that is proportional to the amount of ATP present through the Luciferase reaction. The plates were shaken on an orbital shaker at 100RPM for 10 min at room temperature. Luminescent readouts were obtained using a CLARIOstar plate reader. The cell viability was calculated by subtracting the negative control and blank wells using CellTiter-Glo® 2.0 Assay (Promega). IC_{50} was analyzed based on the log [TAK-981] vs percent of cell viability curve.

2-7 Protein Isolation

KPC-46 cells were seeded in 6-well plates. 1mM TAK-981 was made from 120 mg/ml stock solution. 30 μM and 60 μM TAK-981 in DMSO were made from 1 mM stock. 0 nM, 100 nM, and 200 nM TAK-981 diluted in DMEM complete media were made by adding 10 μl of DMSO, 30 μM, and 60 μM TAK-981 to 3 ml of DMEM complete media. Wells were treated separately with 100 nM, 200 nM TAK-981, no treatment, and 0 nM vehicle control.

2-8 SDS sonication lysis

250μL of 4x Laemmli SDS non-reducing buffer, 50 μl of β-mercaptoethanol, and 750 μl of ultra-purred water were mixed and added to 4 wells of 6-well plate. The cells were scraped and lysed using a sonicator at 20 MHz and 10 seconds four times on ice. Proteins were denatured at 99 °C for 30 minutes.

2-9 Western blot analysis

Denatured proteins were loaded to 12-well NuPAGE™ 4 to 12%, Bis-Tris, 1.0–1.5 mm, Mini Protein Gels(Invitrogen, NP0329BOX) in 1X NuPAGE™ MES SDS Running Buffer (Invitrogen) for 80V, 30 minutes and 120V 60 minutes total. Proteins were transferred onto a nitrocellulose membrane (Invitrogen, Nitrocellulose/Filter Paper Sandwich, 0.2 µm, 8.3 x 7.3 cm) in ice cold 1X NuPAGE™ Transfer Buffer at 4 °C, 90V, 90 minutes. Specific antibodies to SUMO2/3 (1:1000, ab3742, Abcam), GAPDH (1:1000, 97166, Cell Signaling) were detected using the 1:10000 fluorescent secondary antibodies (Licor) and visualized by the Odyssey detection system (Licor).

2-10 Transfection

Lentiviral transfection of 6 µg transfer vector pHIV-Luc-Zsgreen (pHIV-Luc-Zsgreen was a gift from Bryan Welm (Addgene plasmid # 39196 ; http://n2t.net/addgene:39196; RRID:Addgene_39196)) and 2 µg of each pMD2.G (pMD2.G was a gift from Didier Trono (Addgene plasmid # 12259 ; http://n2t.net/addgene:12259 ; RRID:Addgene_12259)), pRSV-REV(*26*) (pRSV-Rev was a gift from Didier Trono (Addgene plasmid # 12253 ; http://n2t.net/addgene:12253 ; RRID:Addgene_12253)), and pMDLg/pRRE(*27*) (pMDLg/pRRE was a gift from Didier Trono (Addgene plasmid # 12251 ; http://n2t.net/addgene:12251 ; RRID:Addgene_12251)) were performed using 14 µl DNA transfection reagent (Lipofectamine™ 2000 Transfection Reagent, Invitrogen) to in 586.55 µl OPTI-MEM (Gbico) and incubated for 30 minutes at room temperature. HEK293T cells were about 60% confluent, and the media was changed before drop-wisely adding DNA-Lipid complexes onto it. After 48 hours, the media was collected and fresh DMEM complete media was added to the HEK293T cells. After 24 hours, the media was collected and combined with previous media. The media was filtered using a 0.45 µm filter unit and concentrated using 10,000 MilliporeSigma™ Amicon™ Ultra-15 Centrifugal Filter Units. The concentrated virus was aliquoted and stored at -80°C.

2-11 Lentiviral transduction of murine PDAC cell line and cell sorting

KPC-46 cells were seeded in a 10 cm dish and were 80% confluent. Collected viruses were added to the target KPC-46 cell line. Cells were monitored to check whether they expressed green fluorescence from the Zsgreen gene. After observation, cells were digested using Accutase (Invitrogen) and resuspended in PBS, no calcium, no magnesium (Gbico) in 2.5 mM EDTA

(Invitrogen), 25 mM HEPES (Invitrogen), pH 7.0, 1% Heat-Inactivated Fetal Bovine Serum (Corning). The resuspended cells were filtered through 0.45 µm. Cell sorting was conducted with an ARIA I cell sorter at La Jolla Immunology Flow Core using FITC and PE channels. Sorted cells were collected and seeded back to a 6-well plate for expansion. Expanded KPC-Luc-Zsgreen cells were used for further *in vivo* mouse injection.

2-12 In vivo experiments

KPC-46-Luc-Zsgreen cells were cultured in a 15-cm dish and digested using Trypsin(Invitrogen). Cells were resuspended in PBS and stored on ice. Each mouse was injected 100 µl with 10,000 KPC-46-Luc-Zsgreen cells. For anesthesia, ketamine was purchased from UCSD Controlled Substance Use Authorization. Ketamine/xylazine was made (K, 100 mg/kg; X, 10 mg/kg) before mouse surgery. Before surgery, the mouse was placed in a chamber containing isoflurane and each mouse received 100 µl of Ketamine/xylazine intraperitoneally. While waiting for full anesthesia, heating pads were applied to keep the mouse warm during surgery covered by absorbance pads to maintain sterility as a surgical platform. After anesthesia, the mouse was placed on the surgical platform and the left subcostal area of the incision was sensitized with 70% ethanol and then iodine. A small incision was made below the left side rib and through the peritoneum using a scissor. Then a Kocher incision was made, and the spleen was taken out using a forceps. 100 µl KPC-46-Luc-Zsgreen cells suspended in PBS were drawn into a 26 G x 5/8" syringe. Cells were injected slowly into the exposed spleen and a whitening spot on the spleen should be observed at the injection site indicating a successful injection of tumor cells. The injection site was cauterized to prevent bleeding of the mouse spleen. Kocher incision was closed using Vicryl (Polyglycolic Acid), Ethicon, Suture, Size: 6-0 (J492G). 3M

Vetbond Tissue Adhesive was applied to close the skin of the mouse. After surgery, 0.1 mg/kg buprenorphine (obtained from UCSD Controlled Substance Use Authorization) was administered intramuscularly injected into mice to alleviate post-surgical pain. All the mice were observed after surgery for five days.

The control mice and treated mice were intraperitoneally injected with vehicle control and TAK-981 24 hours before surgery. The vehicle was made with 20% Kolliphor and 5% dextrose, and autoclaved. For the treated group, 15 mg/KG/animal was diluted in 100 µl vehicle. From day 2, the control mice and treated mice were intraperitoneally injected with vehicles or TAK-981 until day 20.

2-13 Luciferase *in vivo* imaging

D-Luciferin (VivoGlo™ Luciferin, *In Vivo* Grade) was thawed at room temperature and dissolved in DPBS, no calcium or magnesium, (Gbico) to a final concentration of 15 mg/ml and filtered through a 0.22 µm filter. Mice were intraperitoneally injected with D-Luciferin. After 10 minutes, mice were placed in the IVIS 200 machine for *in vivo* bioluminescent imaging at D position, medium spinning, and 2 seconds. ROIs were selected at the ventral sites Photons/s/cm^2/sr.

2-14 *In vivo* mouse analysis

After 20 days, all the mice were euthanized by placing them in a chamber filled with Carbon Dioxide. Peripheral blood was collected from mice by injecting the 26 G x 5/8” syringe into the heart and mixed with 20 µl EDTA (Corning) to prevent clotting. Spleens were collected and placed in ice-cold PBS. Livers were collected and cut in half. Half was placed in a cascade in 4% formaldehyde for Histology and another for tumor dissociation.

2-15 PBMC isolation by Density Gradient Centrifugation

Mouse peripheral blood with EDTA was diluted with an equal amount of Dulbecco's PBS (Corning) with 2 % FBS (Corning). Diluted blood was layered on top of 1mL Lymphoprep™ without mixing them and spun down at 800 xg for 20 minutes at room temperature. By Density Gradient Centrifugation, the blood was separated into plasma, PBMCs, Lymphoprep™, Granulocytes, and red blood cells. PBMCs were collected and stained with Zombie yellow in PBS for 15 minutes at room temperature, and later stained with target antibodies, CD3, CD4, CD8, CD44, CD62L, NK1.1 (Biolegend). The cells were washed with cell staining buffer (Biolegend) and resuspended in 150 µl of cell staining buffer for flow cytometry.

2-16 Flow Cytometry

PBMC cells were first stained with Zombie yellow (Biolegend, 423104) to stain dead cells by resuspending 1µl of Zombie yellow in 100 µl of PBS for one test and incubating in the dark for 15 minutes at room temperature. Cells were washed with 2ml cell staining buffer (Biolegend, 420201) each and spun down at 300 g for 5 minutes. Supernatants were discarded and cells were stained with CD8 (PE-Cy5.5, Biolegend, 100710), CD45 (BV650, Biolegend, 103151), CD3 (APC-Cy7, Biolegend, 100222), CD4 (FITC, Biolegend, 100406), NK1.1 (APC, Biolegend, 108710) antibodies in a total volume of 100µL cell staining buffer each in dark for 15 minutes at 4°C. Cells were washed with 2mL of cell staining buffer and spun down at 300 g for 5 minutes. Supernatants were discarded and cells were resuspended in 300 µl of cell staining buffer.

2-17 Liver and Spleen tumor dissociation

Mice livers were dissected and cut into 2-4 mm pieces and placed in the buffer solution containing 2.35 ml DMEM, high glucose, GlutaMAX™ Supplement, pyruvate (Gibco) in 100 µl of Enzyme D, 50 µl of Enzyme R, and 12.5 µl of Enzyme A into a gentleMACS C tube (Miltenyi Biotech, 130-096-730). Tubes were placed in the gentleMACS dissociator for Tough tumor type and 37C_m_TDK_2 setting program. After dissociation, samples were resuspended in a 15 ml tube and washed with 10 ml of DMEM. Cells were spun down at 300 g for 7 minutes and supernatants were aspirated. Cells were further analyzed using flow cytometry. Fluorescent tumor cells were gating using PE (Blue, 572/28) and FITC (Blue, 525/45) channels.

2-18 Liver fluorescent imaging

Dissected TAK-981 treated, PBS control, and vehicle control mice livers were placed on 10-cm dishes and imaged in IVIS200 using a GFP fluorescence filter. PBS control livers were set as a background to eliminate autofluorescence. Regions of interests (ROIs) were selected at Photons/s/cm^2/sr. The ROIs of TAK-981 and vehicle control liver were calculated by subtracting the ROI values from PBS control mice liver.

2-19 Hematoxylin and eosin stain (H&E) Immunohistochemistry (IHC)

Dissected livers were cut in half, placed in cassettes, and merged in 4% formaldehyde (Thermo Scientific Chemicals, J60401.AK) for 24 hours. Liver tissues were taken out and placed in 70% ethanol. Samples were embedded and H&E staining were done by the Moores Cancer Center Histology core. Blocks were further cut and stained using anti-CK19 (Millipore Sigma, MABT913) and F4/80 (offered by LJI) at La Jolla Institute for Immunology.

2-20 Aldefluor assay for cancer stem cell testing

The Aldefluor kit (StemCell Tech) was used to test KPC-46 cells that express ALDH activity. 10,000 KPC-46 cells were suspended in Aldefluor assay buffer containing 5μL BODIPY-aminoacetaldehyde for each sample and incubated for 30 min at 37 °C. Control samples were stained with an ALDH inhibitor, 5 μl of diethylaminobenzaldehyde, for ALDH activity gating. After 30 min incubation, cells were washed with Aldefluor assay buffer, and the supernatants were discarded. The cells were resuspended in 100 μL of Aldefluor assay buffer and the ALDH bright cells were counted using flow cytometry. The ALDH bright cells activity is detected by a fluorescent green emission 488 nM laser, 525/45 channel tested by Agilent Novocyte Advanteon.

2-21 Statistical analysis

Values are reported as the mean ± SEM. Statistical analyses were performed using GraphPad Prism. Unpaired t-test was used in two groups comparison, and one-way ANOVA followed by Tukey's multiple comparison test more than two groups. Multiple unpaired t-test was used for multiple grouped analyses. $P < 0.05$ was considered as statistically significant.

CHAPTER 3: RESULTS

3-1 Commercial TAK-981 characterization through LC-MS and NMR spectrum

The commercially available TAK-981 was ordered from Chemitek. Before starting *in vitro* or *in vivo* experiments, commercial TAK-981 characterizations using LC-MS and NMR spectra were performed. We compared the purity and molecular weight of commercial TAK-981 from Chemitek with Takeda Pharmaceuticals using Liquid chromatography-mass spectrometry (LC-MS). LC is a chromatographic separation technique. Directly coupled to the mass spectrometer (MS), ionized samples are separated by positive and negative charges (*28*). The charged and differentiated samples can be analyzed by mass/charge ratio (*28*). In the process of identifying or quantifying a peak, it is crucial to ensure that the measured area or height corresponds solely to a single compound. Validation of the integrity of a compound is crucial for result downstream *in vitro* and *in vivo* experiments by assessing both compound purity and concentration.

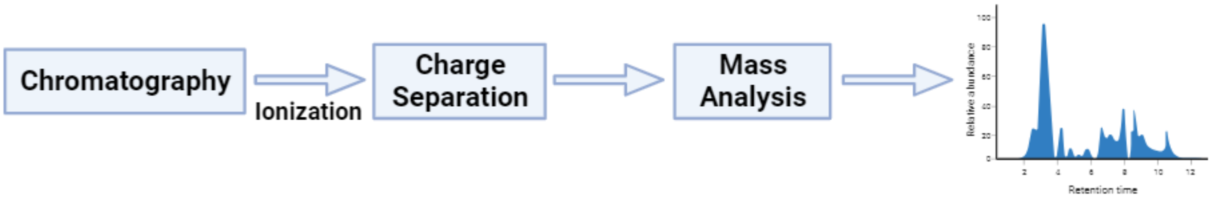

Figure 6. Analytical workflow of Liquid chromatography-mass spectrometry.

Both samples were prepared at a concentration of 1 mg/ml. TAK-981 samples from Takeda Pharmaceuticals exhibited a peak area of 923.452 with a purity of 98.7% as a reference (Fig. 7). In contrast, the commercial TAK-981 displayed a peak area of 883.857 with a purity of 97.6% (Fig. 8). Thus, the commercial material is sufficiently pure. The comparison of peak area between standard (TAK-981 from Takeda Pharmaceuticals) and the commercial TAK-981 suggests that the commercial product is slightly less concentrated than expected by weight, approximately 98% of the calculated concentration by weight.

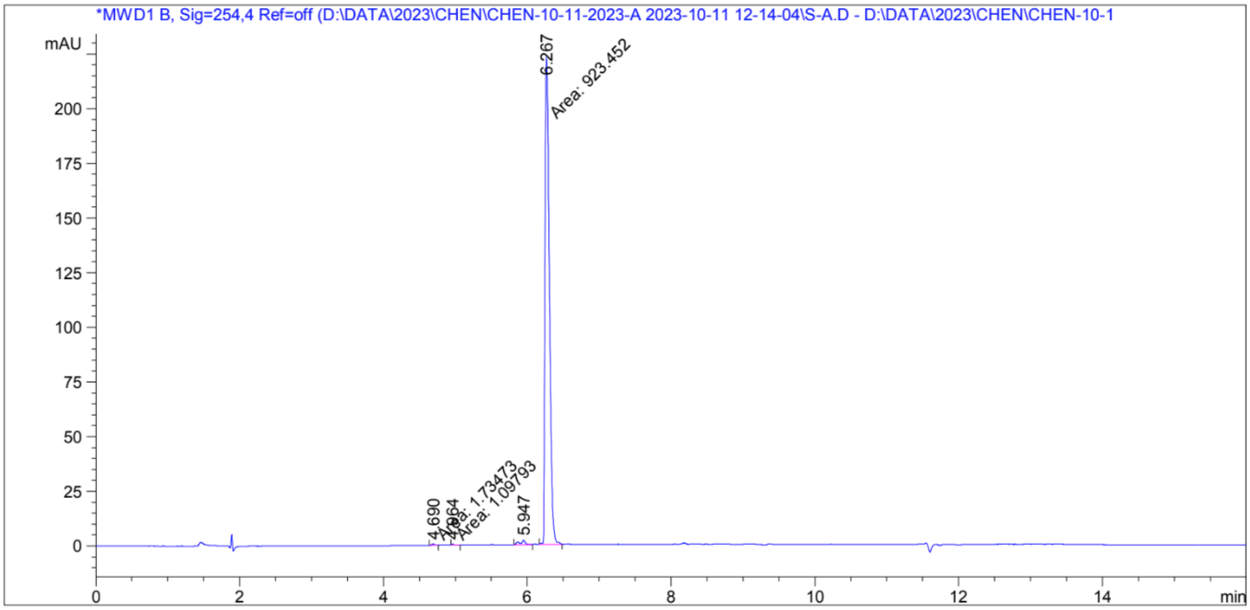

Figure 7. LC of Takeda Pharmaceuticals' TAK-981 sample at a concentration of 1mg/ml.

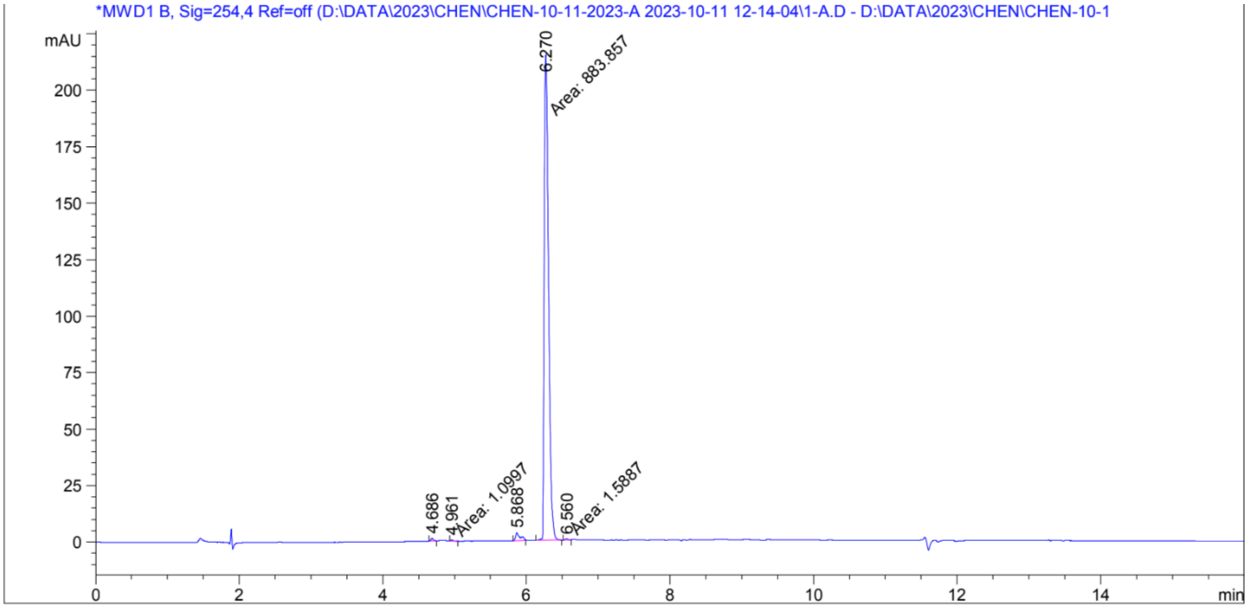

Figure 8. LC of the commercial TAK-981 sample at a concentration of 1mg/ml.

Table 1. Analysis of standard and commercial TAK-981 using liquid chromatography.

	Peak #	RetTime [min]	Width [min]	Area [mAU*s]	Height [mAU]	Height Area %	[M+2H]	$[M+2H]^{2+}$
Standard	4	6.267	0.0692	923.45221	222.52658	98.6671	578.09	289.85
Commercial	4	6.270	0.0685	883.85736	214.96834	97.5741	578.10	289.85

The Mass spectrum (MS) data exhibited a similar molecular ion with the addition of a single proton [M+H] of 578.09 for the standard and 578.10 for commercial TAK-981. The molecular ion with the addition of two protons and a double positive charge $[M+2H]^{2+}$ also expressed same value: 289.85 (Fig. 9 and 10). Those multiple charge states confirmed of the identity of the commercial TAK-981 by comparing to the standard.

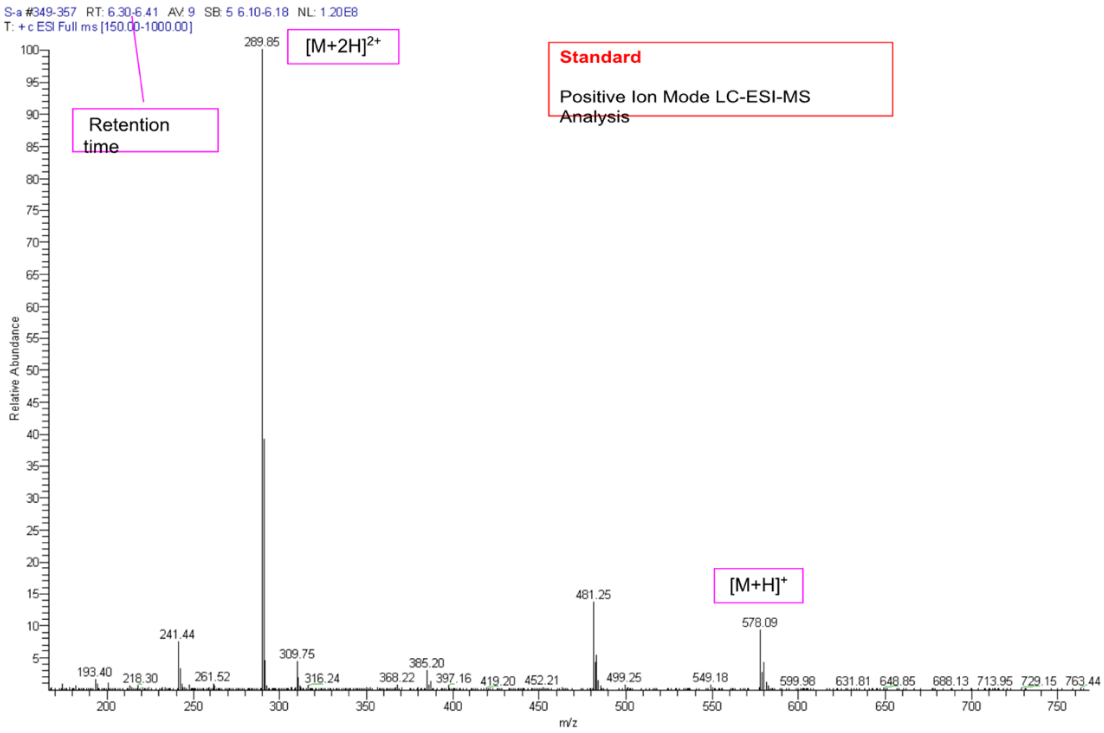

Figure 9. MS of Takeda Pharmaceuticals TAK-981 samples at a concentration of 1mg/ml.

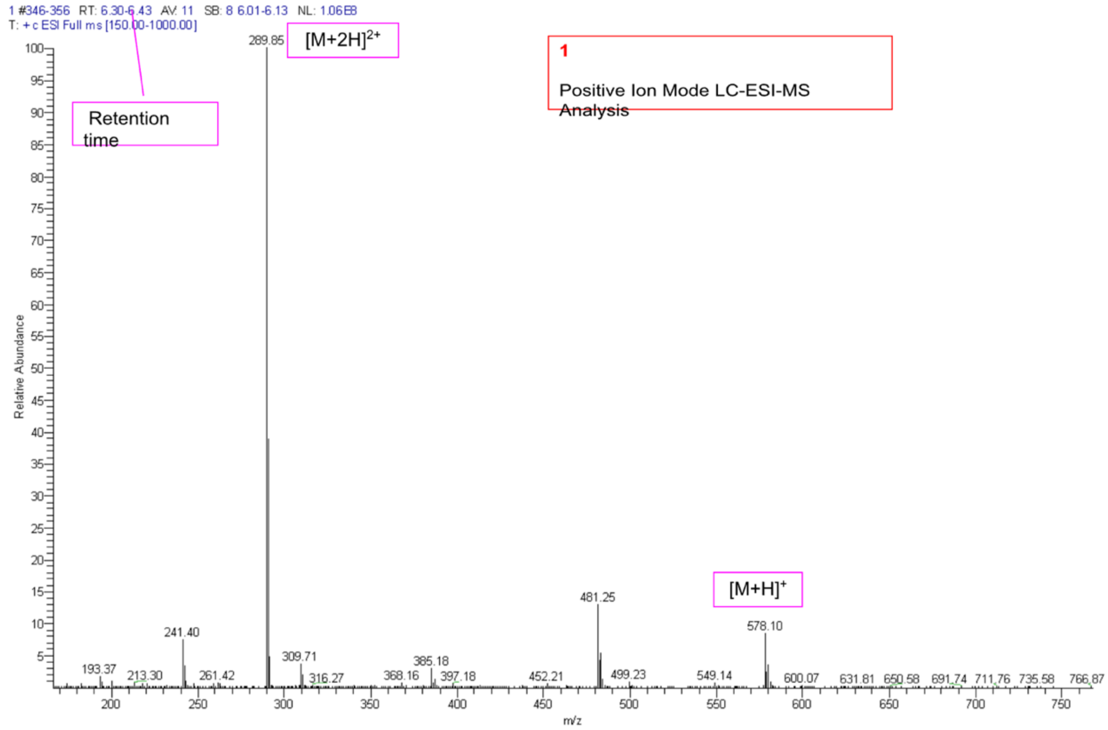

Figure 10. MS of Commercial TAK-981 samples at a concentration of 1mg/ml.

We utilized LC-MS to assess the degradation of TAK-981 in water over 1, 24, and 48 hours. Purity measurements revealed values of 96.7446%, 95.8108%, and 94.4763% at 1, 24, and 48 hours, respectively (Table 2). Distinct peaks were observed at retention times of 6.264, 6.264, and 6.258 minutes, respectively. Notably, no additional peaks emerged after 24 and 48 hours, suggesting the absence of new UV absorbing degradation products (Fig. 11 - 13). This lack of additional peaks and consistent multi-charged state (Fig. 14 - 16) provide evidence that TAK-981 may be stable in aqueous environment beyond 24 hours well, within the timeframe of *in vitro* experiments and drug preparation for *in vivo* dosing. In summary, our time-course experiment demonstrates the stability of TAK-981, persisting for more than 24 hours in the aqueous solution.

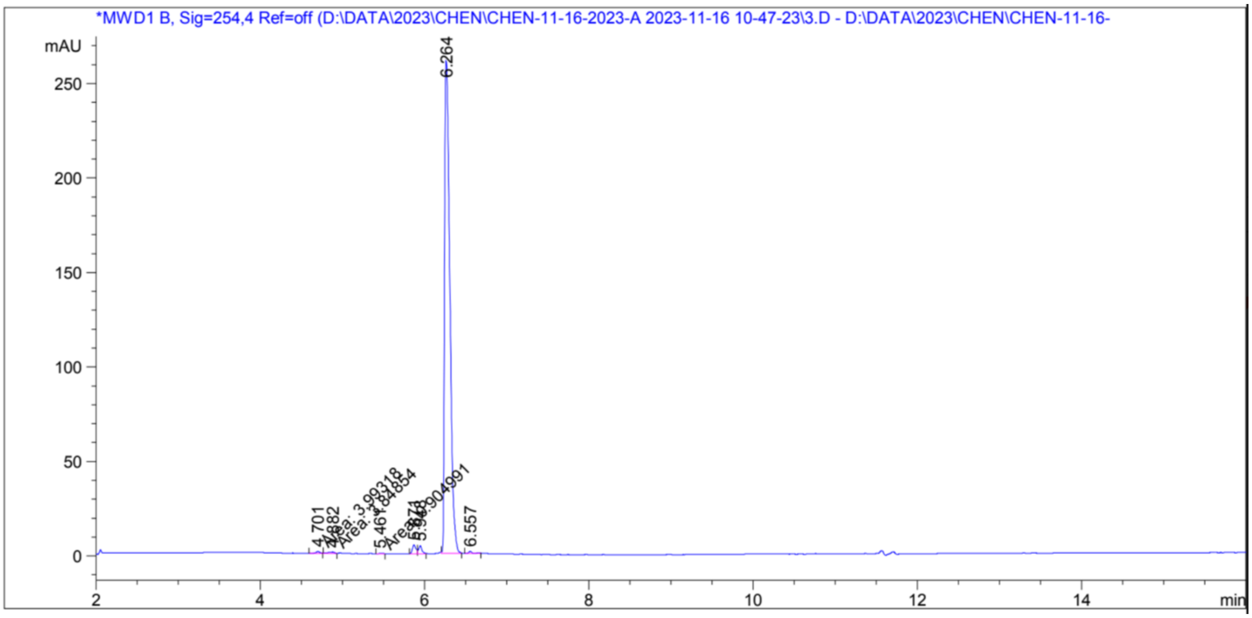

Figure 11. LC of Commercial TAK-981 samples at a concentration of 1mg/mL in 1h.

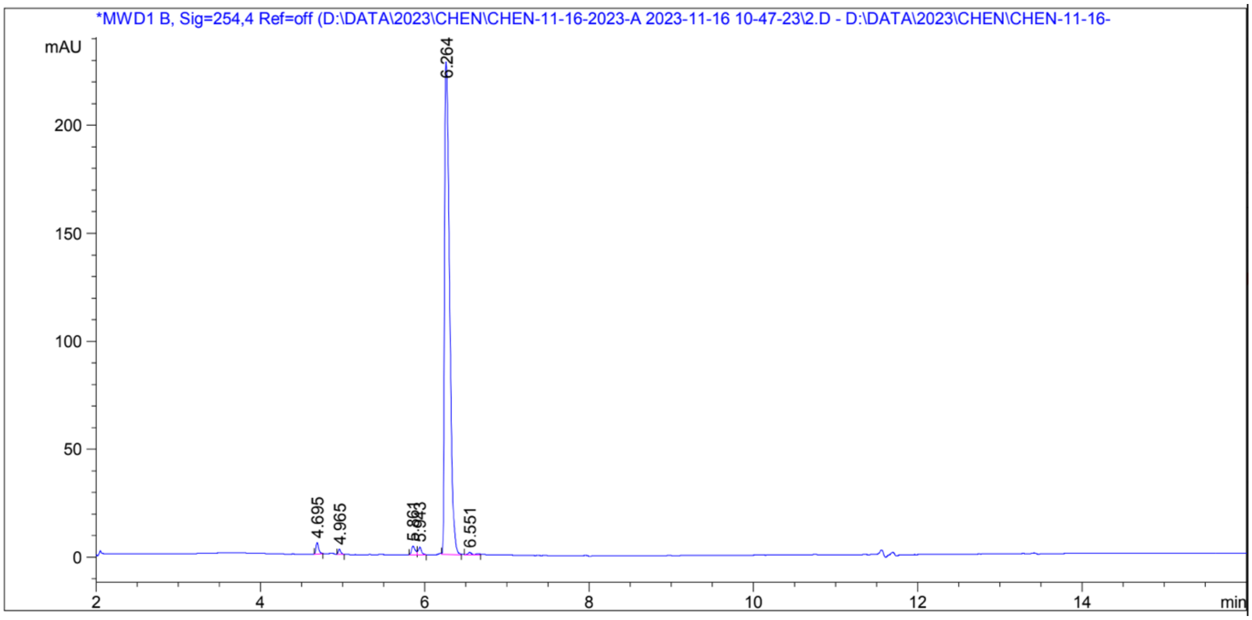

Figure 12. LC of commercial TAK-981 samples at a concentration of 1 mg/mL in 24h

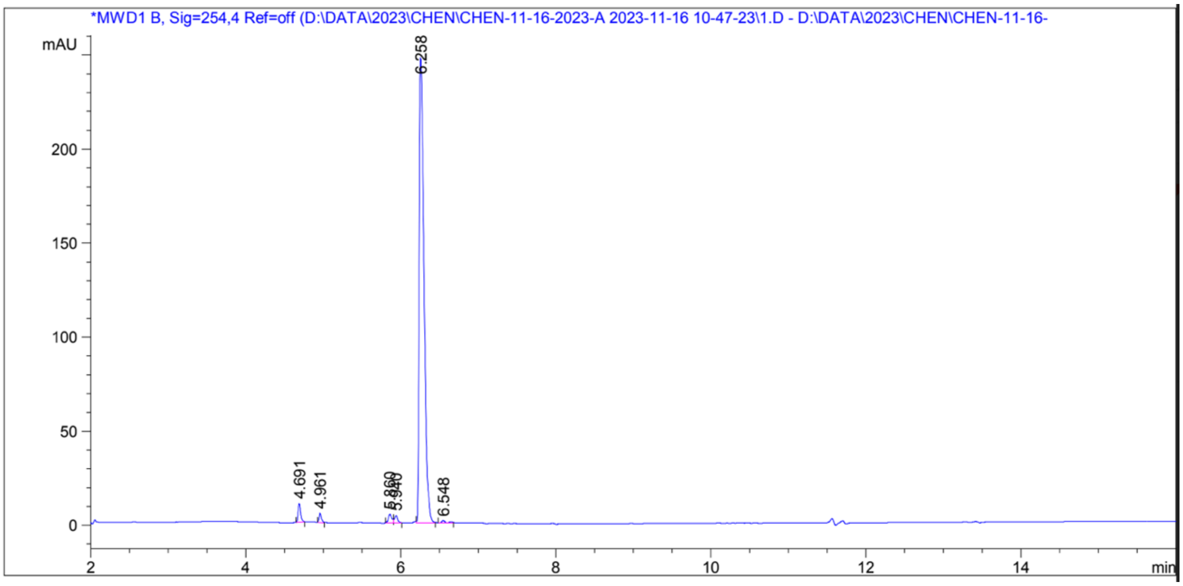

Figure 13. LC of commercial TAK-981 samples at a concentration of 1 mg/mL in 48h.

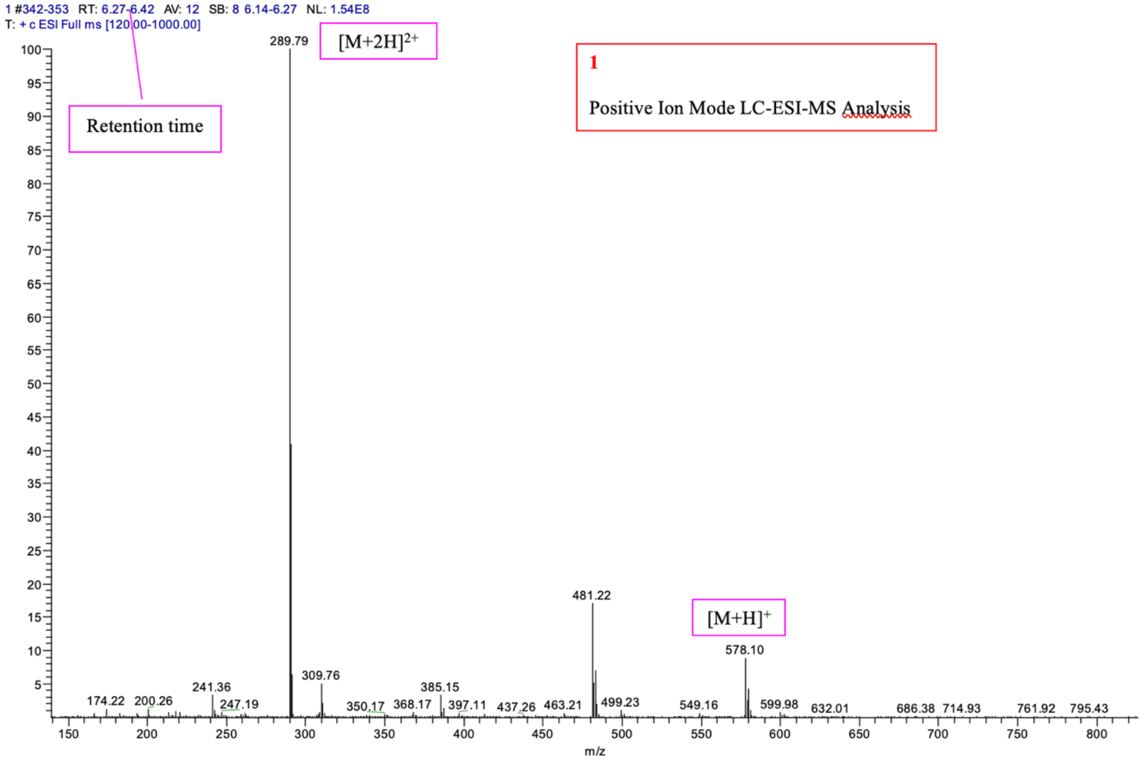

Figure 14. MS of commercial TAK-981 samples at a concentration of 1 mg/mL in 1h.

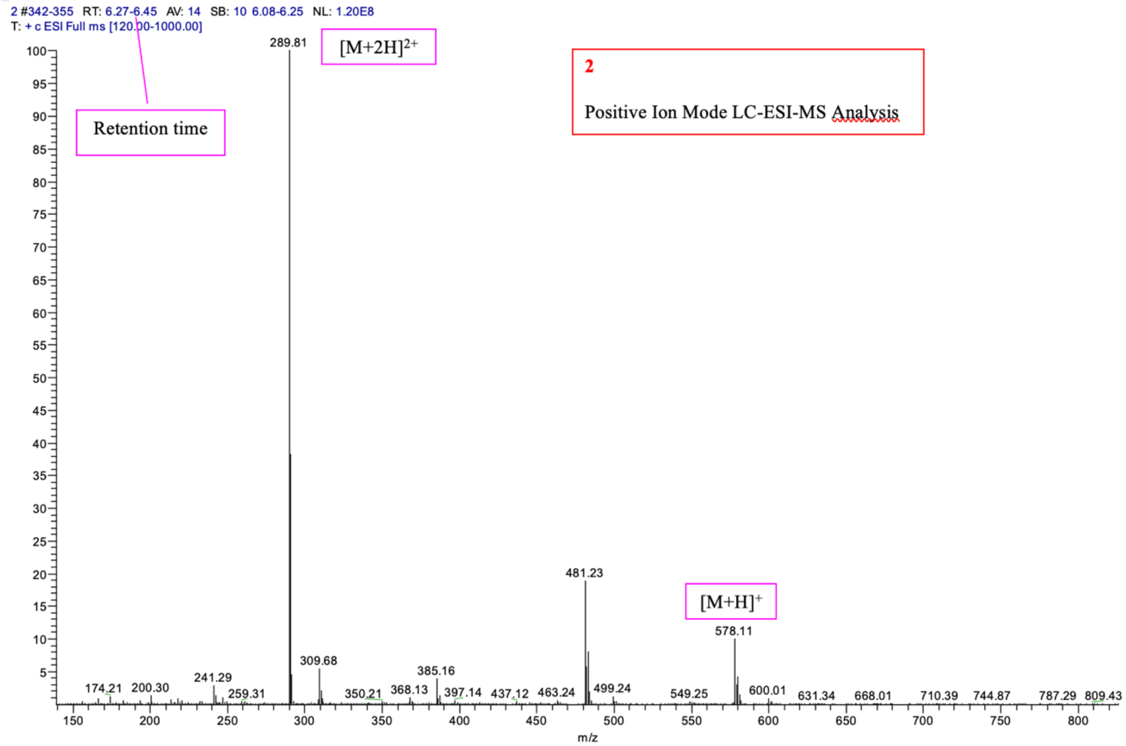

Figure 15. MS of commercial TAK-981 samples at a concentration of 1 mg/mL in 24h.

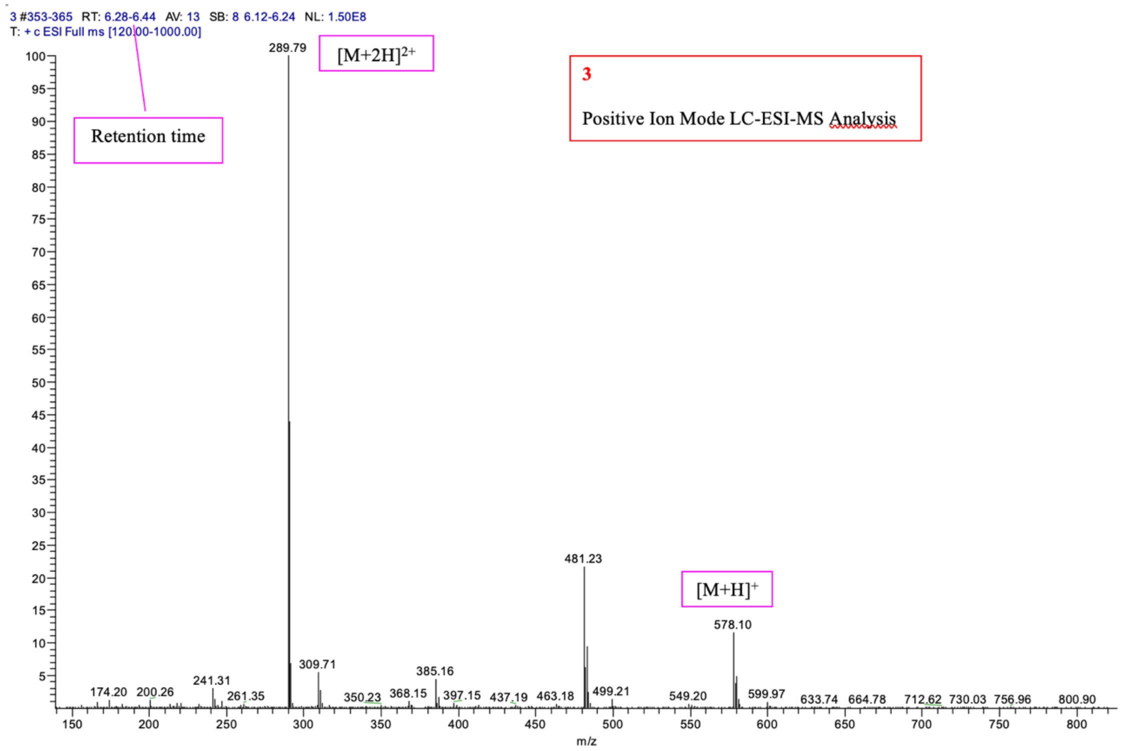

Figure 16. MS of commercial TAK-981 samples at a concentration of 1 mg/mL in 48h.

Table 2. Analysis of commercial TAK-981 in 1h, 24h, and 48h.

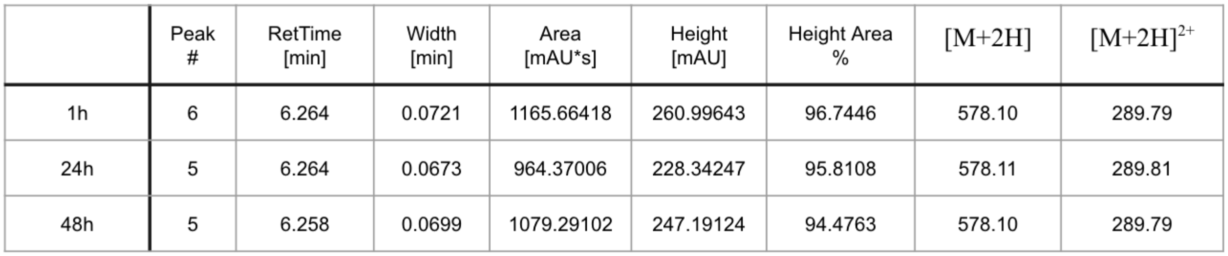

	Peak #	RetTime [min]	Width [min]	Area [mAU*s]	Height [mAU]	Height Area %	[M+2H]	$[M+2H]^{2+}$
1h	6	6.264	0.0721	1165.66418	260.99643	96.7446	578.10	289.79
24h	5	6.264	0.0673	964.37006	228.34247	95.8108	578.11	289.81
48h	5	6.258	0.0699	1079.29102	247.19124	94.4763	578.10	289.79

Nuclear magnetic resonance spectroscopy (NMR) is a technique to determine the structure of molecules. Numerous nuclei exhibit spin and carry an electric charge, as outlined by the principles of NMR (*29*). By subjecting a sample to an external magnetic field, energy transfers from the base energy to a higher level which then alters the resonance frequency of an atom within a molecule, influenced by the intramolecular magnetic field encompassing it (*29*). NMR detects the signals arising from the relaxation processes. This alteration provides insights into the specific functional groups and structure of the molecule. Additionally, NMR is employed to assess the stability of a compound over time due to its ability to provide detailed information about the molecular structure (*30*). Alterations in the chemical shifts of NMR spectrum can indicate variations in the compound's structure or degradation over time (*29*, *30*). By examining the ^1H NMR spectrum of TAK-981 at various time points, the comparative analysis offered insights into the stability of TAK-981 over time.

We also characterized TAK-981 by diluting the 120 mg/mL stock TAK-981 to a concentration of 1 mM in D_2O. The NMR spectrum is consistent with the molecular structure of TAK-981. The observed chemical shifts and coupling patterns are aligned with the expected values based on the known structure and functional groups within TAK-981 as shown in Fig. 17. For example, the aromatic region, from 5.82 to 8.51 ppm, shows the resonances of seven singlet protons, consistent with the TAK-981 structure (*9*).

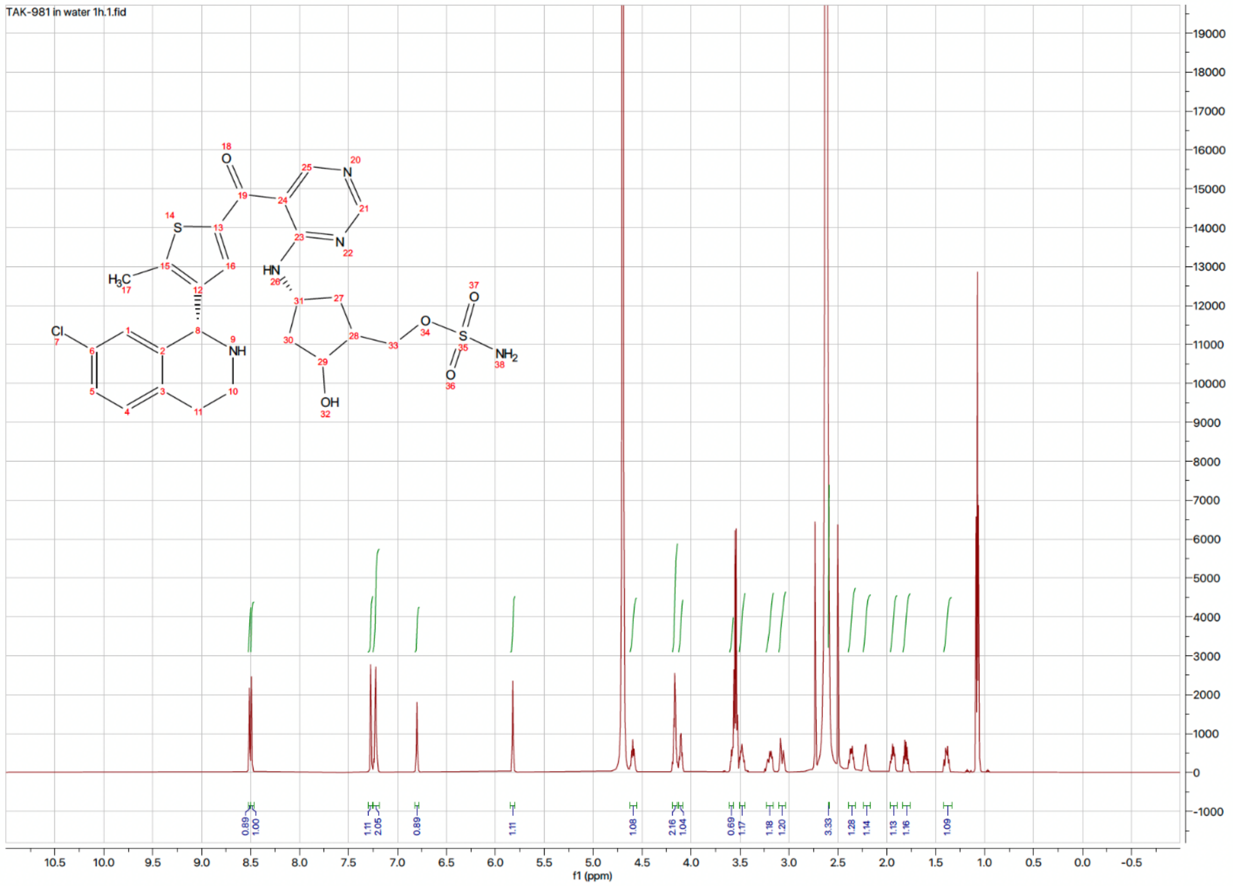

Figure 17. NMR spectrum of 1mM commercial TAK-981 in D_2O.

The stability test results indicate that the chemical shifts with integral values of TAK-981 after 24 hours closely resemble the original TAK-981 spectrum (Fig. 18).

The NMR data align with the LC-MS data, collectively demonstrating that the purity of Chemitek TAK-981, ensuring that any effects observed in later *in vitro* and *in vivo* experiments are attributable to TAK-981 itself rather than any impurities in the drug. Furthermore, the structural integrity assessed through NMR and LC-MS indicates the stability of Chemitek TAK-981 in aqueous solutions for a minimum of 24 hours. These characterizations offer insights into the strategy for subsequent treatment.

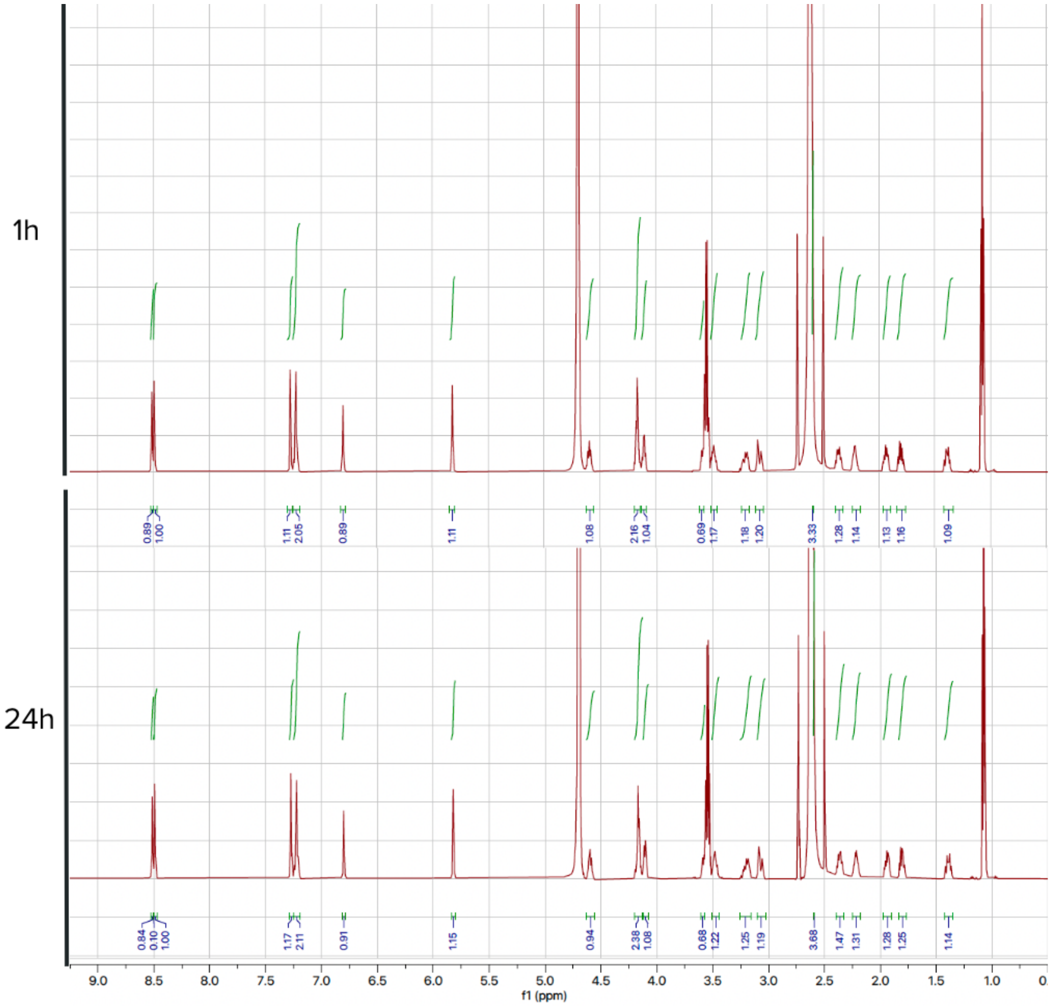

Figure 18. NMR spectrum of TAK-981 diluted in D_2O for 1 hr and 24 hr.

3-2 Validating SUMOylation inhibition using TAK-981 in KPC-46 cell line.

Following the drug characterization, we focused on assessing the effectiveness of TAK-981 in inhibiting SUMOylation within the KPC-46 cell line by treating the cells with various concentrations of TAK-981, followed by an analysis of SUMO2/3 protein expression levels. Notably, the overall expression of SUMO 2/3-conjugated proteins showed a significant decrease following treatment after 25 nM of TAK-981 (Fig. 19). These findings strongly indicate that TAK-981 effectively inhibits the SUMOylation in the KPC-46 cancer cell line even at 12.5 nM concentration.

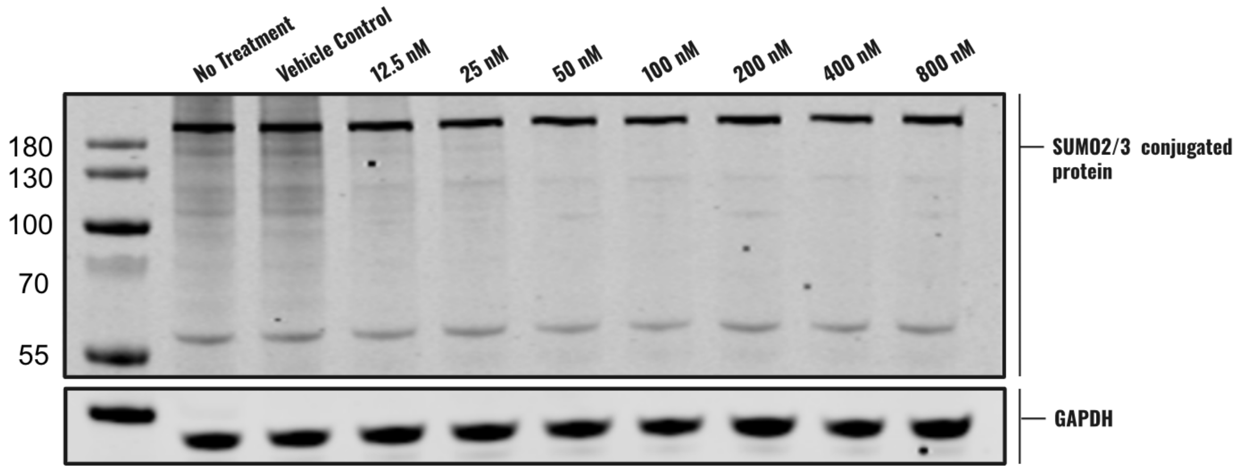

Figure 19. SUMO2/3 protein expression level of KPC-46 cells after 24 hours.

3-3 Investigating the metastatic niche formation after TAK-981 treatment.

We continued exploring the development of metastatic niches to facilitate tumor cell colonization, specifically on the communication between cancer cells and liver stomal cells after TAK-981 treatment. Tumors can initiate the development of microenvironments in distant organs which can further promote the survival and proliferation of tumor cells (*31*). The expression of pro-inflammatory cytokines can recruit the bone-marrow derived cells to establish this pro-tumor niche formation (*31*). An experiment involved administering TAK-981 or vehicles to KPC-46 cell line, co-cultured with harvested hepatic stellate cells (HSCs) from the mouse liver. mRNA were extracted from the HSC for RT-qPCR analysis. As depicted in Fig. 20, notable reductions in CCL20 and IL6 expression were observed in HSC after TAK-981 treatment in mice. This implies that TAK-981 induced alterations in several pro-inflammatory cytokines, including chemokines and interleukins which in turn further altered the tumor cell interactions with the primary liver stromal cells in metastatic niche formation in PDAC liver metastasis.

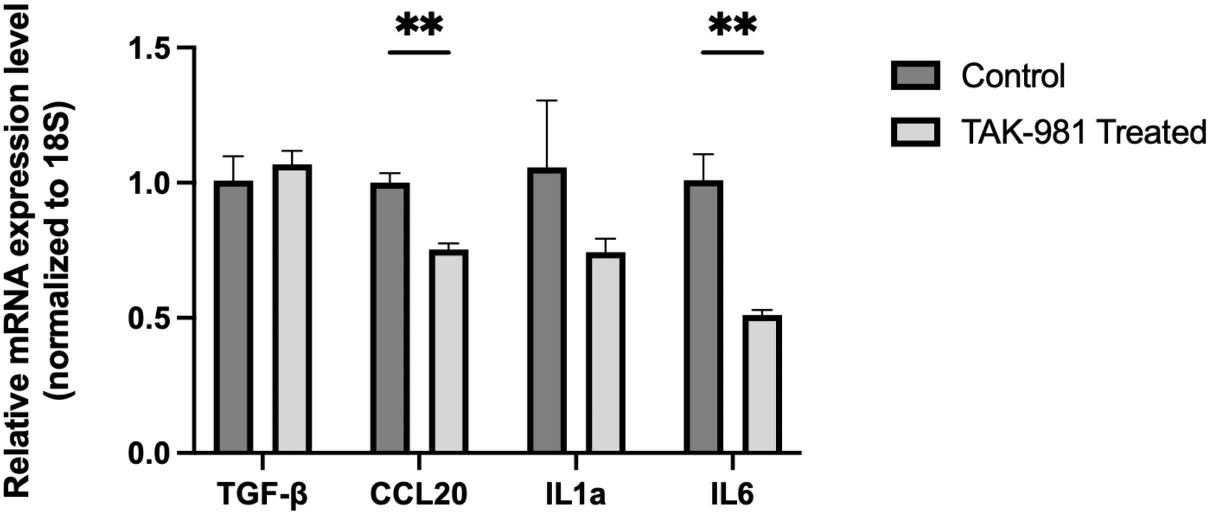

Figure 20. Effect of TAK-981 on communication between KPC-46 cancer cells with HSC.

3-4 Stable reporter KPC-46 cell line engineering for *in vivo* imaging.

To image and quantify the KPC-46 cells in mice, a stable reporter KPC-46-Luc-Zsgreen was developed using lentiviral transduction. Transfection of viral vectors into HEK293T cells allow the production of lentiviral vectors. The lentiviral vector is constructed on the foundation of HIV-1, incorporating the envelope (Env) protein VSV-G. The virulence gene was knocked out and replaced with an exogenous target gene. Group Antigens (Gag) form the viral core and polymerase (Pol) carries out reverse transcriptase taking the RNA genome to double-stand DNA, together with the Regulator of expression of virion proteins (REV), resulting in the assembly of a 3rd generation lentiviral packaging system (*32*). We achieved a stable expressing line by lentiviral transduction (Fig. 21).

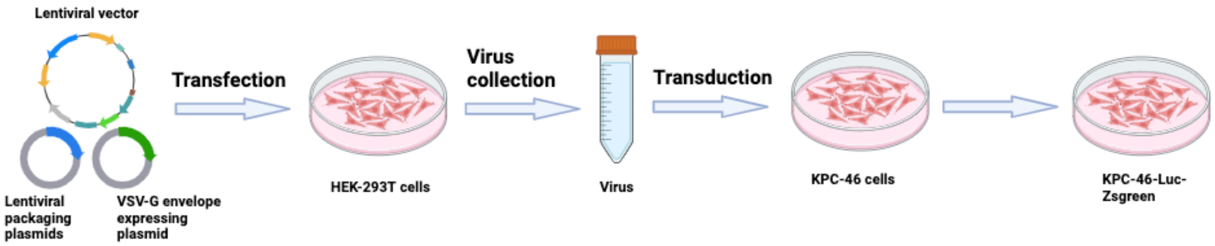

Figure 21. Graphic summary of Lentiviral transfection and transduction pathway.

The pHIV-Luc-Zsgreen plasmid (Fig. 22) comprise the Internal Ribosome Entry Site (IRES), connecting the coding sequences of luciferase and Zsgreen (*33*). This enables the simultaneous expression of luciferase and the green fluorescence protein (Zsgreen) from a single mRNA, enabling straightforward tracking of cell by bioluminescence and fluorescence. By establishing a stable cell line expressing Luciferase/Zsgreen, we achieved real-time imaging capabilities, enabling the monitoring and recording of tumor formation within a living mouse.

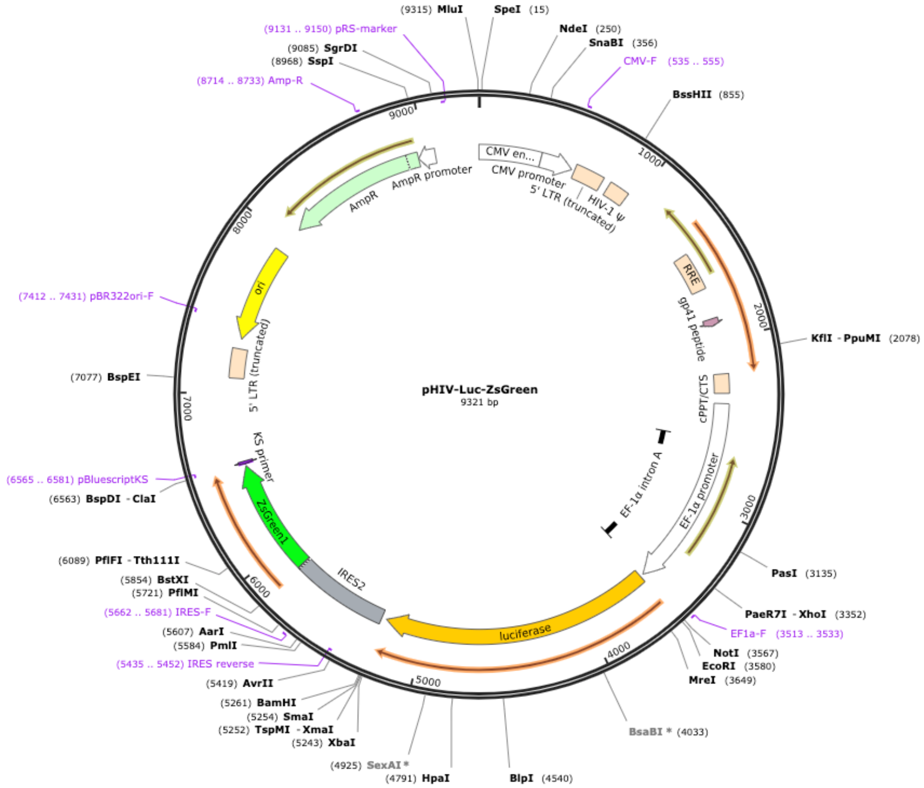

Figure 22. pHIV-Luc-Zsgreen plasmid sequence

In the pHIV-Luc-Zsgreen plasmid, firefly luciferase (FLuc) is employed for *in vivo* tumor cell tracking. Bioluminescence is generated from the conversion of chemical energy to light through luciferase enzymes and their substrates, D-luciferin, within living organisms (Fig. 23)(*34*). Intraperitoneal administration of D-Luciferin in mice facilitates the generation of robust bioluminescent signals (*34*). Consequently, KPC-46-Luc-Zsgreen, featuring Zsgreen genes for *in vitro* cell observation (Fig. 24) and FLuc gene for *in vivo* imaging of tumor cells, is established.

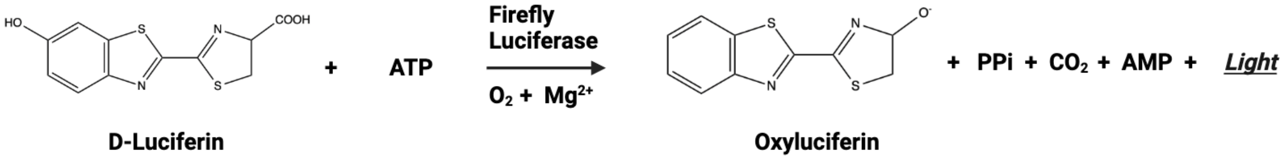

Figure 23. Bioluminescence reactions catalyzed by firefly Luciferase.

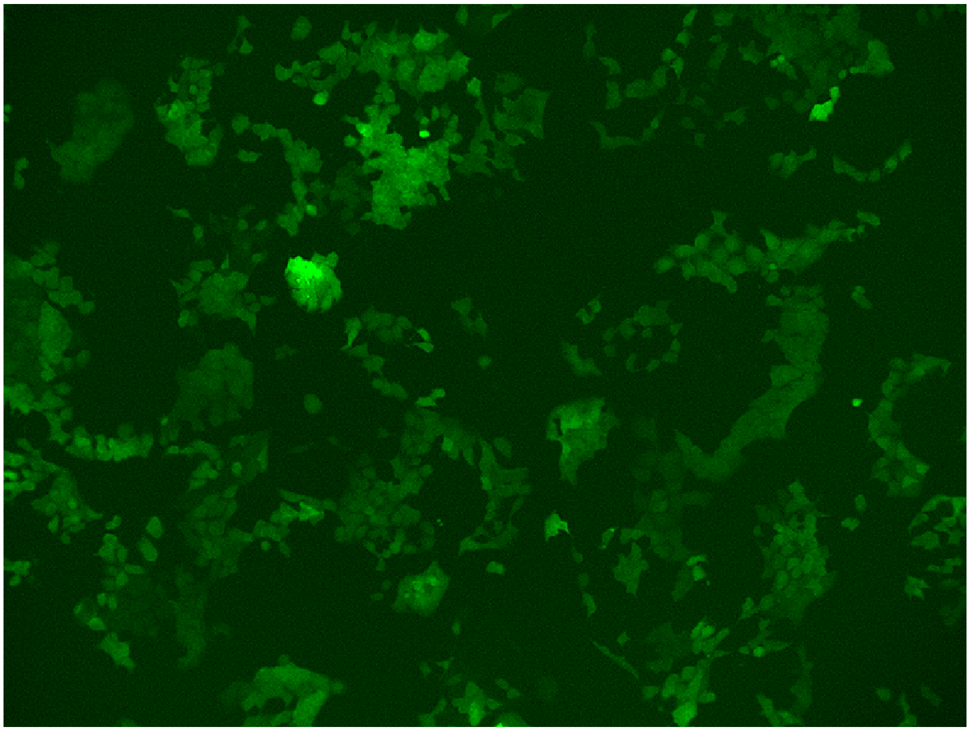

Figure 24. Zsgreen$^+$ KPC-46 cells imaging.

3-5 *in vivo* imaging of mice, liver, and spleen

The orthotopic mouse model was utilized for PDAC analysis. Due to the preliminary examination of HSC mRNA expression level with a decrease in CCL 20 and IL6, the mice were treated with TAK-981 or vehicle control 24 hours before surgery. Following intra-splenic injection, the KPC-46-Luc-Zsgreen tumor formations were monitored on days 4 and 16 during the *in vivo* treatment using bioluminescent imaging. The bioluminescent signal analysis involved selecting the region of interest (ROI) on the ventral site. Quantitatively, on day 4 post-surgery, the cancer cells exhibited a similar and low amount in both the vehicle control and TAK-981 treated groups (Fig. 25 and 26), suggesting a lack of significant expansion at this early stage (Fig. 26). However, as the cancer cells began to proliferate, by day 16, the vehicle control groups displayed higher bioluminescent signals compared to the TAK-981 group (Fig. 25 and 26), indicating that TAK-981 treatment effectively suppressed tumor growth *in vivo*.

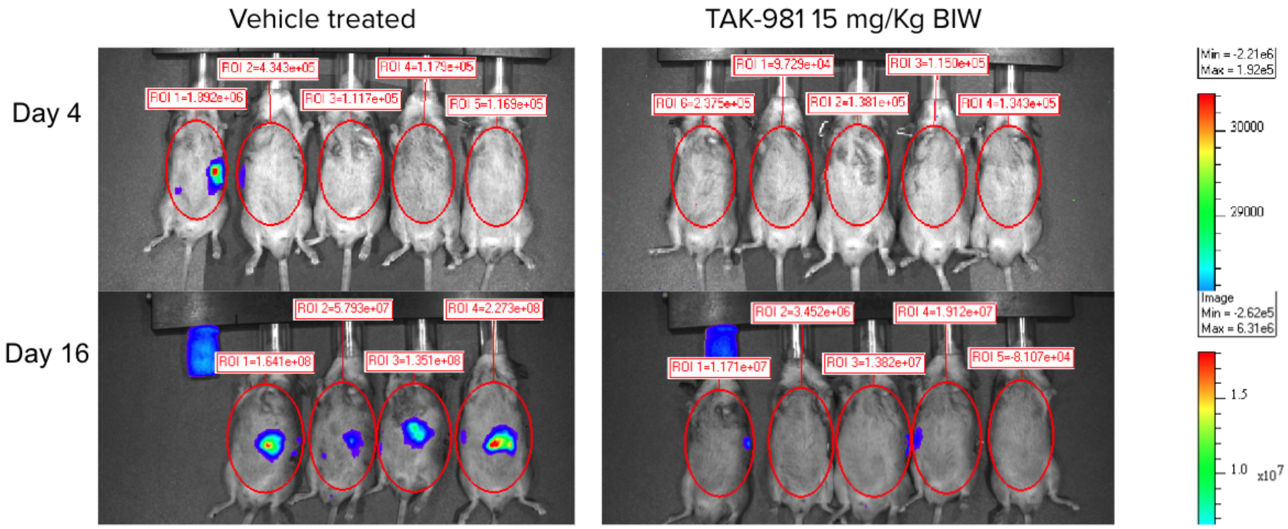

Figure 25. Bioluminescent Imaging of tumor-bearing mice receiving vehicle control or TAK-981 treatment on day 4 and day 16.

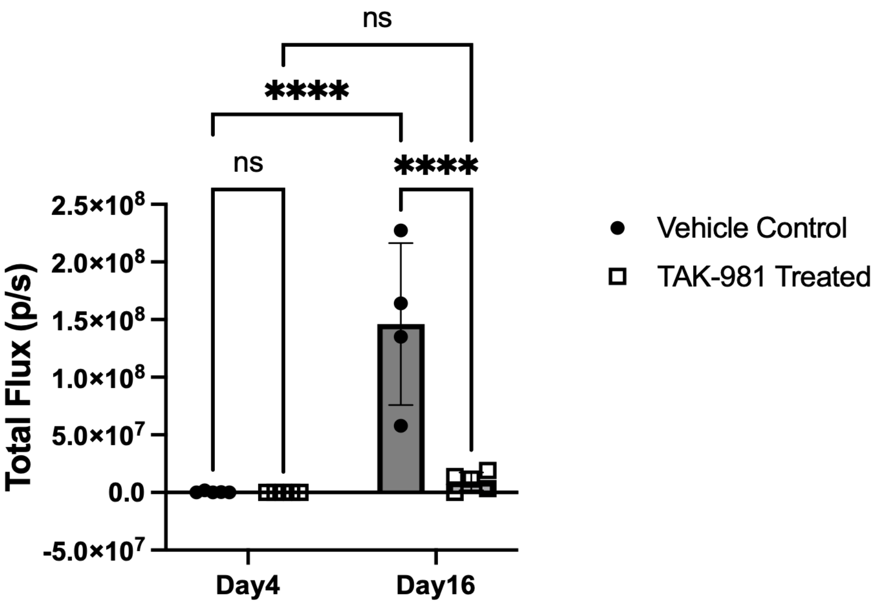

Figure 26. Quantification of Bioluminescent Imaging of tumor-bearing mice receiving vehicle control or TAK-981 treatment on day 4 and day 16. Day 4: Veh: n = 5, TAK: n = 5; Day 16: Veh: n = 4, TAK: n = 5 **** $P < 0.0001$.

On day 20, all mice underwent euthanasia for analysis. We initially compared the direct phenotypic effects of tumor formation in the livers and spleens between the vehicle control and TAK-981 treated groups. Green arrows indicate tumor formation. In the liver, the vehicle control group exhibited evident metastasized tumor formation, whereas TAK-981 treated mice did not show apparent tumor formation in the livers (Fig. 27). Furthermore, the vehicle control group displayed livers with a lighter color compared to both the TAK-981 treated and PBS control healthy mice. This observation is consistent with tumor burden and hypoxia occurs in tumors. In fact, PDAC death is often caused by liver failure due to PDAC liver metastasis.

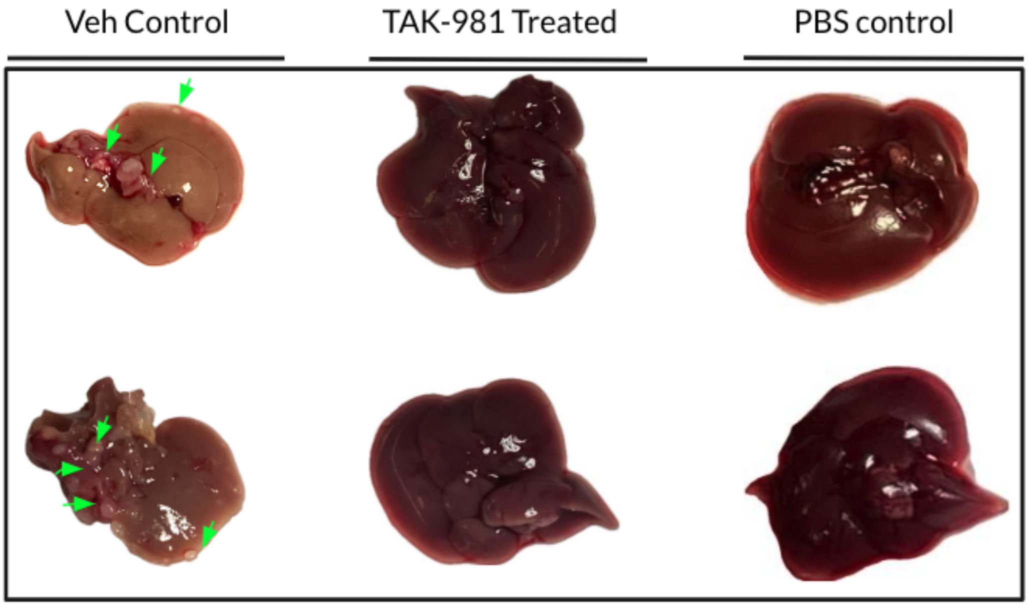

Figure 27. Phenotype of Mice liver on day 20; Green arrows represent the metastasized tumor in the liver.

The spleen, the primary tumor site where cells were injected, displayed significant differences in tumor formation. The vehicle control group exhibited primary tumors that had grown to a size similar to the liver, whereas in the TAK-981 treated group, tumor formation was minimized, and the size resembled that of the original spleen (Fig. 28). This suggests that the TAK-981 treatment has diminished the tumor formation in both the liver metastatic site and the spleen primary tumor injection sites.

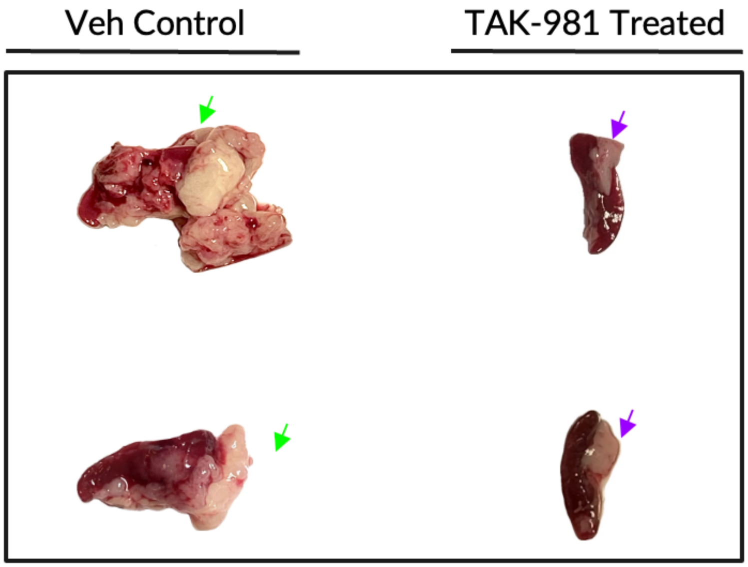

Figure 28. Phenotype of Mice injection site: spleen on day 20. Green arrows represent the tumor formations in the primary injection site in the vehicle control group, and purple arrows represent the tumor in the TAK-981 treated group.

For a detailed analysis of liver metastasis in this mouse model, the Zsgreen fluorescence within the mice livers were monitored. The red spots, representing Zsgreen fluorescent signals, were normalized against the PBS control group to eliminate autofluorescence. In the Fig. 29, the vehicle control group exhibited red spots within the mice's livers, whereas TAK-981 did not display any obvious fluorescence signal, indicating a suppression of liver metastasis following TAK-981 treatment. Quantifying the fluorescent signal by selecting the ROI, the TAK-981 treated group showed a significantly lower signal (Fig. 30). This significant difference is consistent with visual observation that TAK-981 effectively suppresses PDAC liver metastasis *in vivo*.

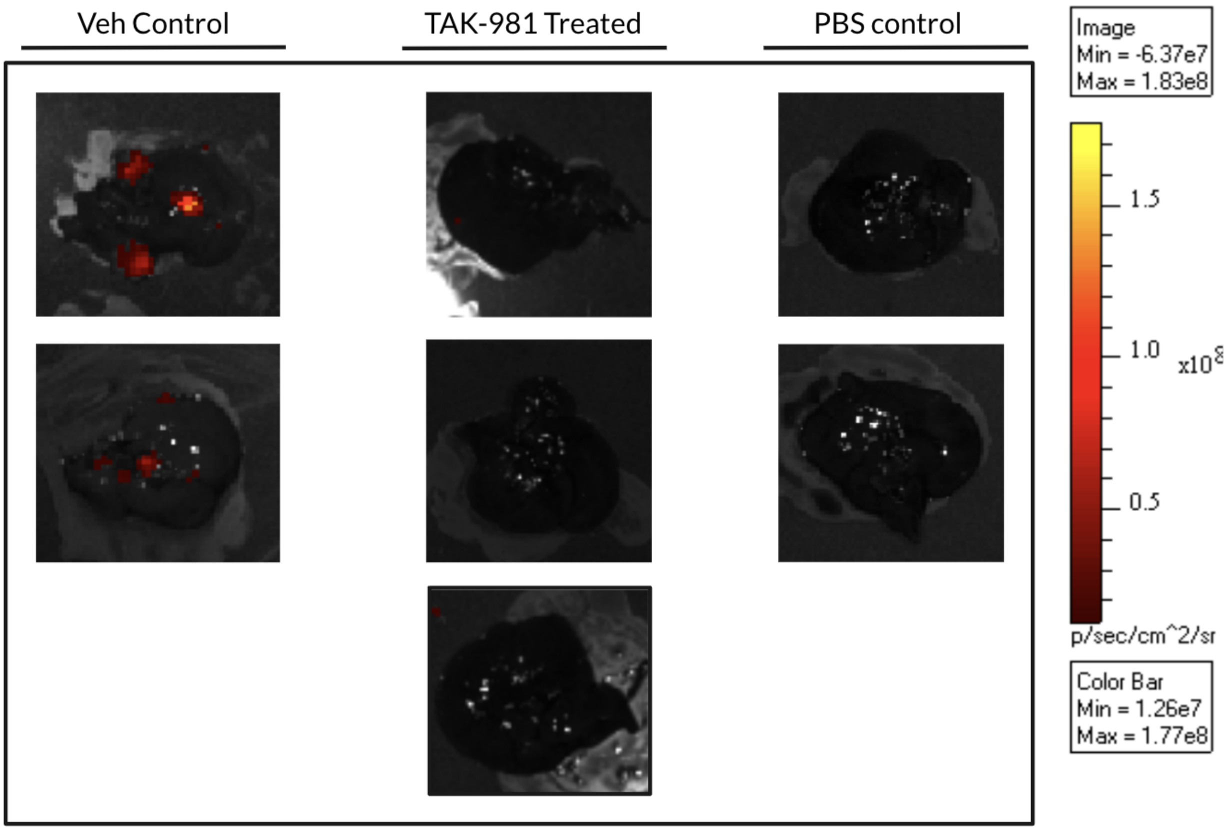

Figure 29. Zsgreen Fluorescent imaging of mice liver receiving vehicle control or TAK-981 treatment on day 20. Regions of interest (ROIs) were designated for both the vehicle control and TAK-981 treated groups, with PBS control groups serving as background 1 (BKG1) and background 2 (BKG2). Data analysis involved subtracting the ROI values by BKG1 and BKG2 for accurate calculation.

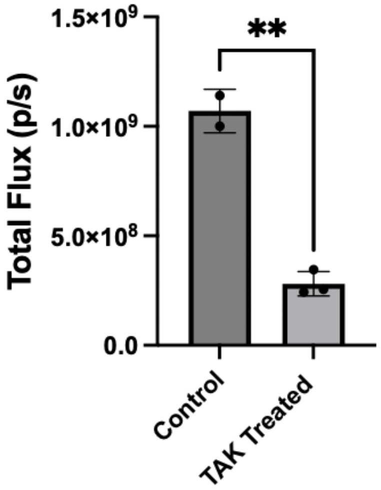

Figure 30. Quantification of Zsgreen Fluorescent imaging of mice liver receiving vehicle control or TAK-981 treatment on day 20 through ROIs. P-value = 0.0013; Veh: n = 2; TAK: n = 3; ** $P < 0.01$.

In addition to bioluminescent and fluorescent imaging with quantification, livers were dissociated, and tumor cells were isolated using flow cytometry for another batch of mice. Due to the Zsgreen gene in the KPC cancer cell line, metastasized tumor cells were isolated using the green fluorophore channels FITC and PE. Using the gating strategy illustrated in Fig. 31, Zsgreen$^+$ cells were gated, representing metastasized tumor cells. Further quantification revealed that in the vehicle control group, the average percentage of Zsgreen$^+$ tumor cells within the liver was 2.593 ± 0.38%, while the TAK-981 treated group displayed only 0.13 ± 0.15% of Zsgreen$^+$ cells (Fig. 32). This indicates a significant reduction in PDAC liver metastasis following TAK-981 treatment.

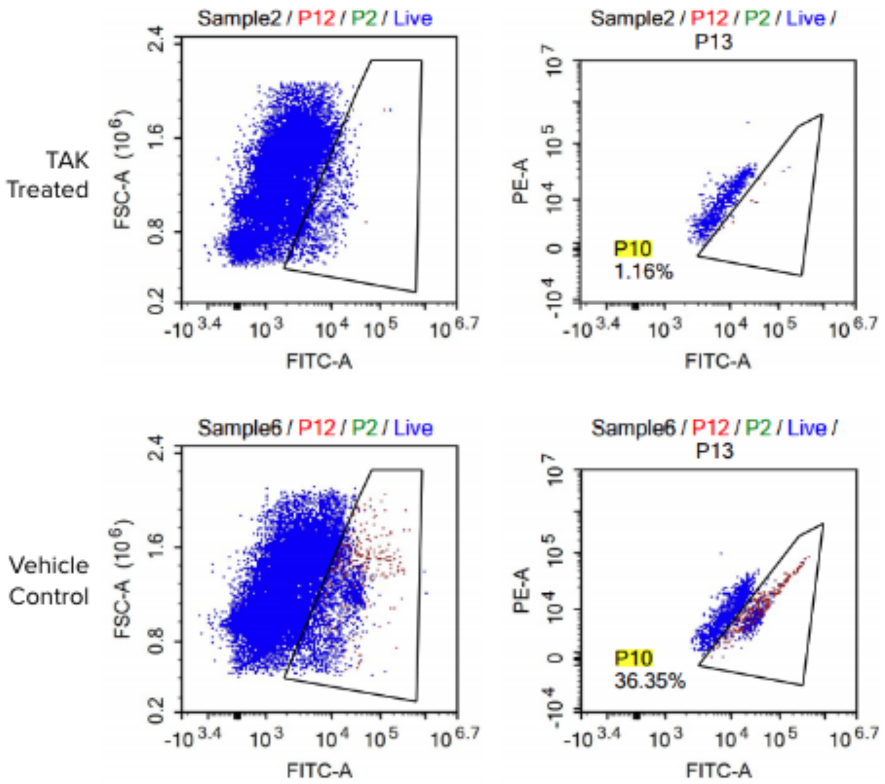

Figure 31. Flow gating strategy using FITC and PE channel for Zsgreen$^+$ cells sorting.

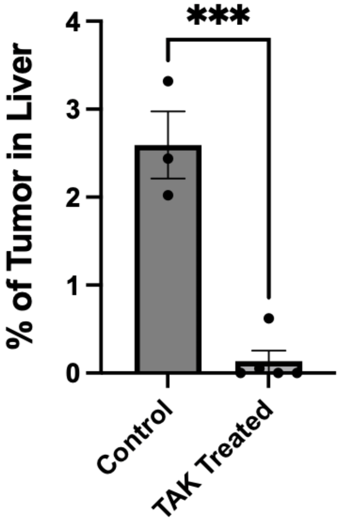

Figure 32. Quantification of Zsgreen$^+$ cells using flow cytometry gating strategy. Veh: n = 3; TAK: n = 5; *** $p < 0.001$.

3-6 *In vivo* immune effect examination on PDAC liver metastasis model

Because SUMOylation is known have an important role in immune response, we proceeded to investigate the impact of SUMOylation inhibition on immune cells. Peripheral blood mononuclear cells (PBMCs) were isolated for the examination of immune effects. Flow cytometry analysis was employed to measure the expression of CD45, CD3, NK1.1, CD4, and CD8 markers in cells. Initially, CD45$^+$ cells were gated from the population of living cells. Subsequently, NK1.1$^+$ and CD3$^{+/-}$ cells were gated specifically from the CD45$^+$ cell population. Finally, within the CD3$^+$ cell subset, further gating was performed to distinguish CD4$^+$ and CD8$^+$ cells (Fig. 33).

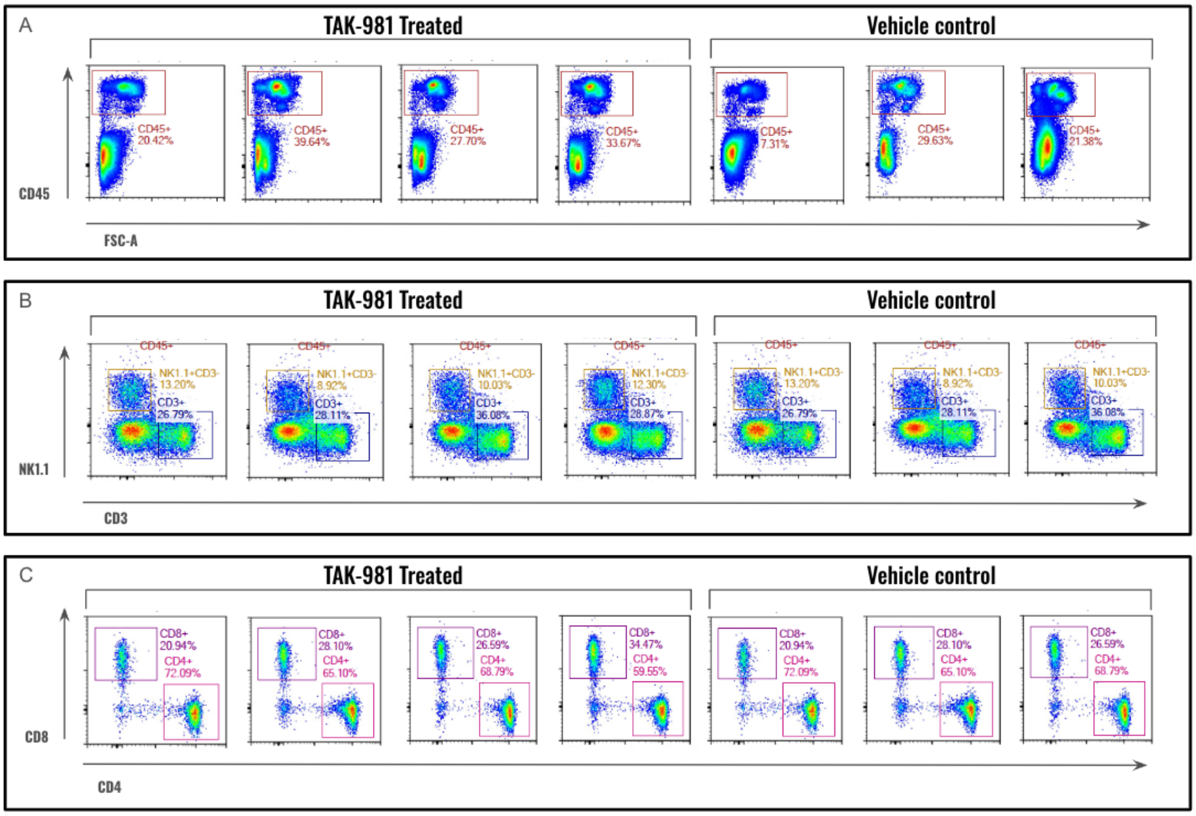

Figure 33: Flow cytometry of immune cells in mouse PBMC. Cells were stained with CD45 (BV650), CD3 (APC-Cy7), CD4 (FITC), CD8 (PE-Cy5.5), and NK1.1 (APC).

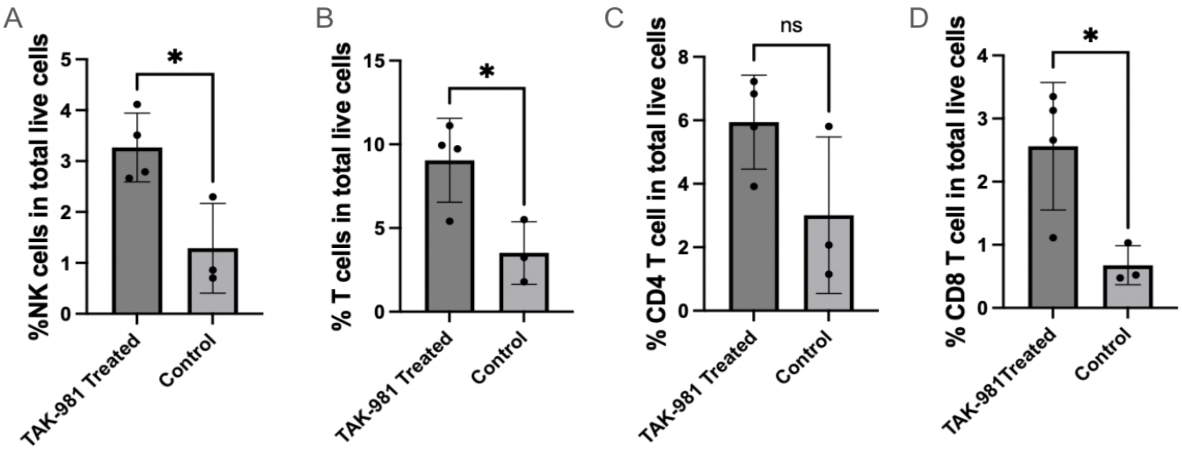

Figure 34. Percentage of NK1.1$^+$ cells(A), CD3$^+$ T cells(B), CD4$^+$ T cells(C), and CD8$^+$ T cells(D) in total PBMC live cells. TAK: n = 4; Veh: n = 3; * $p < 0.05$.

The immune system defense through two main lines of defense: innate immunity and adaptive immunity. Innate immunity is the initial rapid response without immunologic memory.

Adaptive immunity, triggered by specific antigens, requires a longer time exposure, and thus has the capacity of memory formation. By assessing both aspects, the overall immune function was investigated to better understand the immune system's capacity to respond to PDAC liver metastasis.

Nature killer (NK) cells are cytolytic effector lymphocytes linked to innate immunity, which can directly induce the death of tumor cells. In mouse PBMCs, there's an enhancement of NK cell percentage in TAK-981 treated mice compared to vehicle control mice (Fig. 34A).

While innate immunity can directly recognize and kill tumor cells, it can further present foreign antigens to adaptive immune systems. T cells are derived from bone marrow and matured in the thymus (*35*). Linked to adaptive immunity, T cells recognize their antigen after being processed and presented on antigen-presenting cells (*35*). $CD3^+$ T cells contain both $CD4^+$ and $CD8^+$ T cells. After TAK-981 treatment in mice (Fig. 34B), we found an increase in total $CD3^+$ T cells (Fig. 34B). $CD4^+$ cells contain both helper T cells and immune suppressive regulatory T cells (Tregs) (*35*). As depicted in Fig. 32C , TAK-981 did not specifically changed total $CD4^+$ T cell population. On the other hand, $CD8^+$ T cells represent cytotoxic T cells that can target tumor-specific antigens and kill pathogen or neoplastic cells directly (*35*). TAK-981 treatment leads to an increase in $CD8^+$ cytotoxic T cells (Fig. 34D).

$CD8^+$ T cells also develop immunological memory. Memory $CD8^+$ T cells are long-lived and antigen-specific, which means that they can enhance protective response upon encountering the same antigen in subsequent exposures (*35*). Both central memory (Tcm) and effector/memory(Te/m) are derived from naive T cells(Tn). Central memory T cells have the capability to expand to be effective T cells in antigen-specific manner (*36*). CD44 and CD62L (L-selectin) are two surface markers that can define the differentiating subsets in $CD8^+$ T cells in mice: naive T cells (CD44^{low}CD62L^{high}), central memory (CD44^{high}CD62L^{high}), and effector/memory (CD44^{high}CD62L^{low}) (Fig. 35).

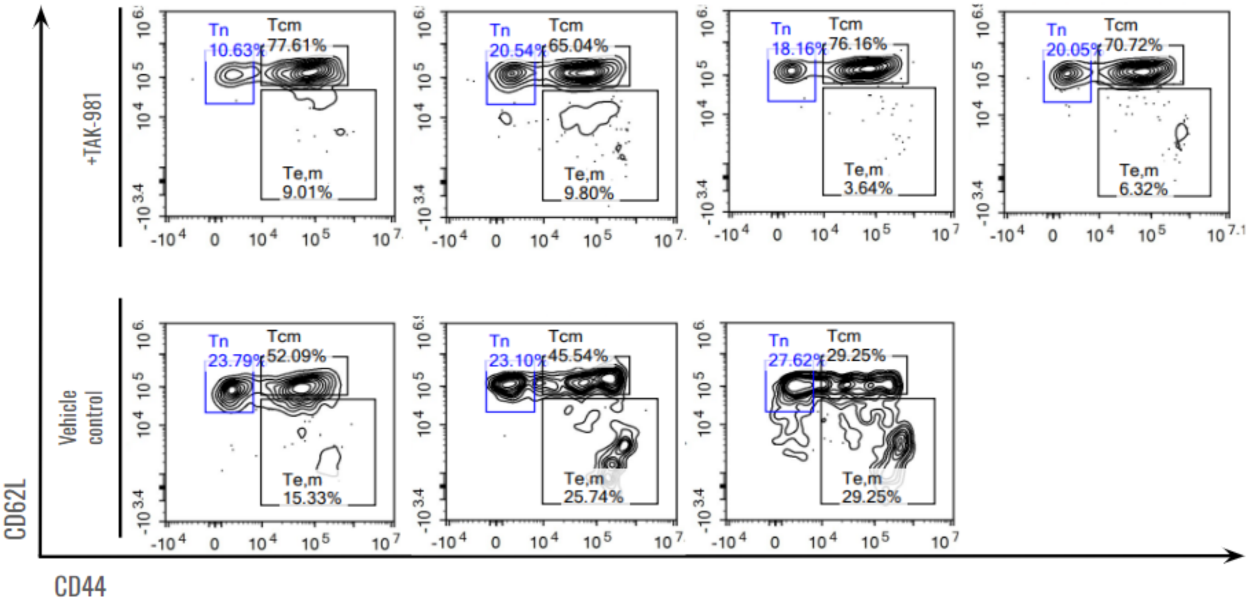

Figure 35. Flow cytometry gating of naive (Tn), central memory (Tcm), and effector/memory (Te/m) T cells within CD8$^+$ T cells population in TAK-981 treated and vehicle control mice.

We found an increase in Tcm and Tn in the total live cells after TAK-981 treatment (Fig. 36A, 36C) while no difference in Te/m in the total live cells (Fig. 36B). The composition of these cells within CD8$^+$ T cells shows the differentiating pattern of Tcm, Te/m, and Tn. Even though the absolute percentage of Tn shows a significant difference, the % Tn in CD8$^+$ T cells has no significant difference (Fig. 36C). However, TAK-981 treatment results in the formation of Tcm rather than Te/m within the CD8$^+$ T cells compared to the vehicle control group. As a result, these data suggest that TAK-981 leads to central memory T cell formation among CD8$^+$ T cells and among all immune cells.

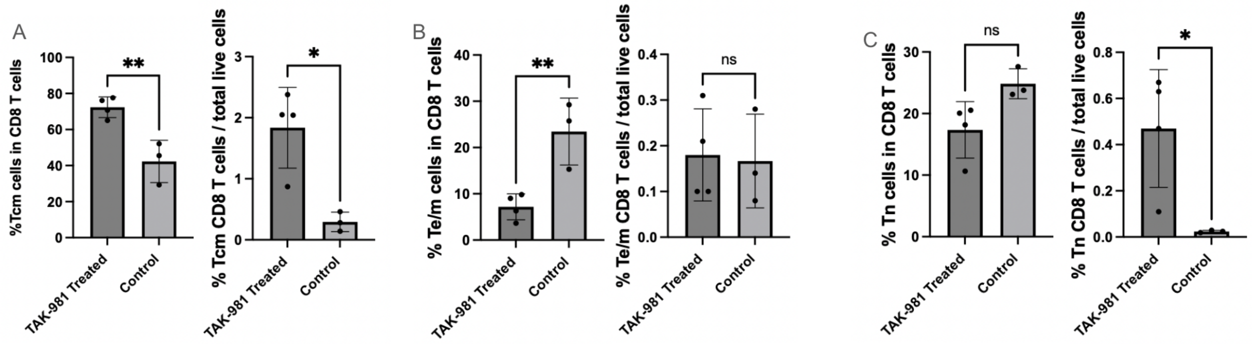

Figure 36. Quantification of Tcm(A), Te/m(B), and Tn(C) in CD8 T cells or total live cells. TAK: n = 4; Veh: n = 3; ** $p < 0.01$; * $p < 0.05$.

Overall, there’s an enhancement in both innate and adaptive immune responses after TAK-981 treatment. These data suggest that TAK-981 has boosted immunity in mice with SUMOylation inhibition treatment.

3-7 Macrophages in Hepatic Tissue

To begin investigating the impact of SUMOylation inhibition on immune infiltration to the liver, I started by staining for macrophages in mouse hepatic tissues. The macrophages can act as tumor infiltration cells to facilitate tumor progression. The magenta, fluorescent signals represent epithelial/tumors using CK19$^+$ markers, the yellow, fluorescent signals represent macrophages using F4/80$^+$ markers, blue fluorescence represents DNA nuclei using Hoechst, and merged of F4/80$^+$ and Hoechst (Fig. 37).

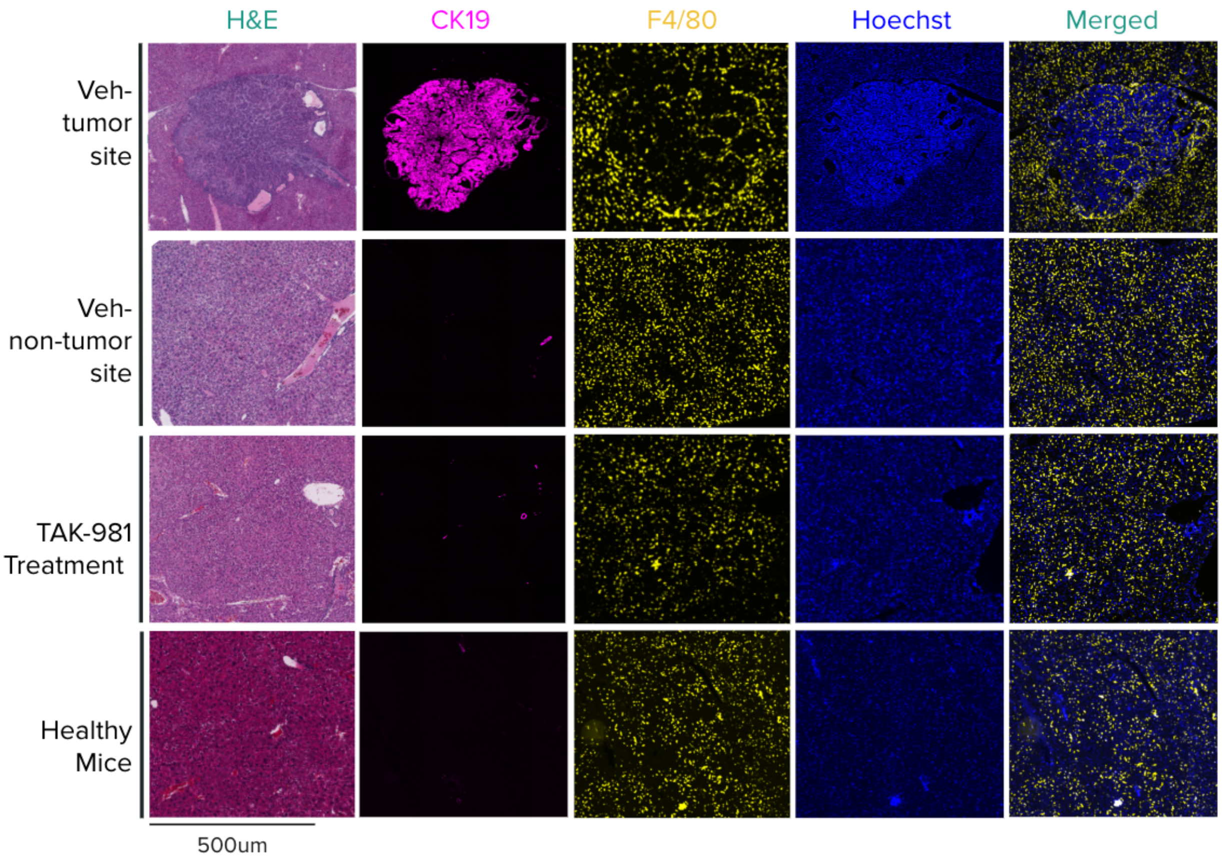

Figure 37. H&E staining and Immunofluorescent staining of CK19$^+$ (epithelial tumor), F4/80$^+$ (macrophages), and Hoechst (DNA).

To quantify the number of macrophages in mice liver, F4/80$^+$ cells were examined by randomly selected five areas in one liver tissue from each group. Mice treated with TAK-981 exhibited similar macrophage numbers as healthy mice in the liver, while vehicle control group has increase macrophages in both tumor and non-tumor regions (Fig. 37 & 38). In addition, there is an increased macrophage population in the tumors than average non-tumor area of a tumor bearing liver, consistent with previous findings that macrophages are highly enriched in PDAC (*37*). This data suggests that the TAK-981 treated mice have liver tissues similar to that observed in healthy mice, consistent with visual observation of liver color (Fig. 25).

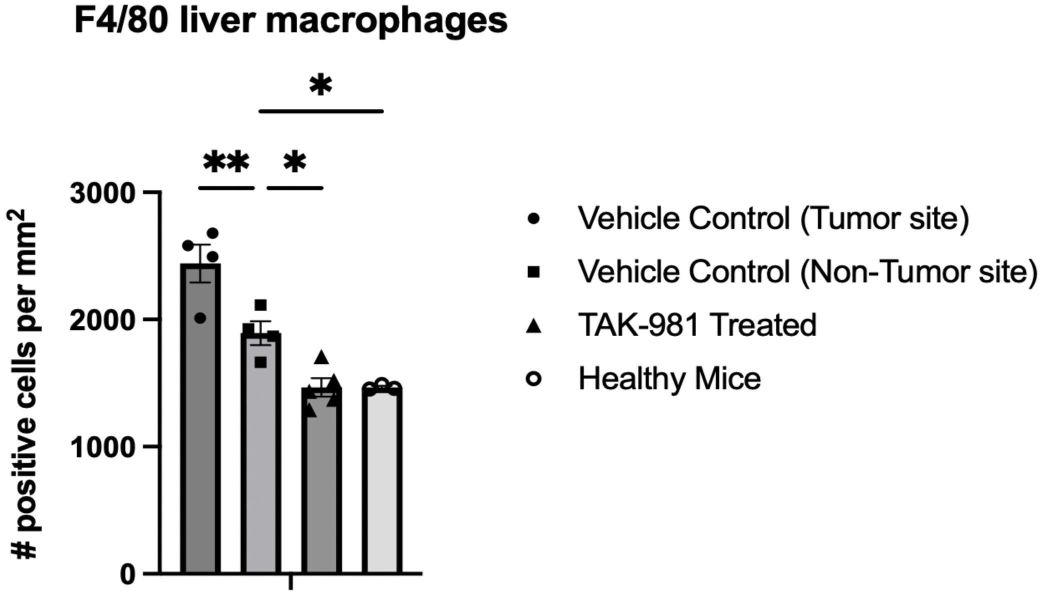

Figure 38. Quantification of the number of macrophages per area(mm^2) in vehicle control tumor site, Vehicle control non-tumor site, TAK-981 treated, and healthy mice liver tissue slides using F4/80$^+$ marker IF staining. Veh: n = 4; TAK: n = 5; Health n = 3 ** $P < 0.01$; * $P < 0.05$.

3-8 *In Vitro* Tumor-Specific Effect on Cancer Cells

We also investigate the potential impact of SUMOylation inhibition on cancer cell viability and cancer stem cells (CSCs). CSCs are a subpopulation of tumor cells with the capacity to initiate tumor initiation at a distal site, causing metastasis. Despite undergoing conventional treatments such as chemo- and radiotherapy, CSCs are able to survive and, in some instances, even exhibit an enrichment (*38*). This resilience underscores the challenge in effectively targeting and eliminating CSCs as part of cancer treatment. Consequently, we examined the *In vitro* tumor-specific effect in the KPC-46 cancer cell line by testing the CSC marker: Aldehyde dehydrogenase (ALDH) through its corresponding substrate.

The efficacy of TAK-981 on the PDAC cell line KPC-46 was examined using CellTiter-Glo using a condition mimicking that of in vivo exposure. We treated the cells at the indicated concentrations of TAK-981 initially for 24 hours and washout the drug by replacing the media following continued culturing for an additional 24 hours an IC50 was found to be 103.5nM to ensure cancer cell death are biologically relevant and lie within the dynamic range of the drug effectiveness (Fig. 38).

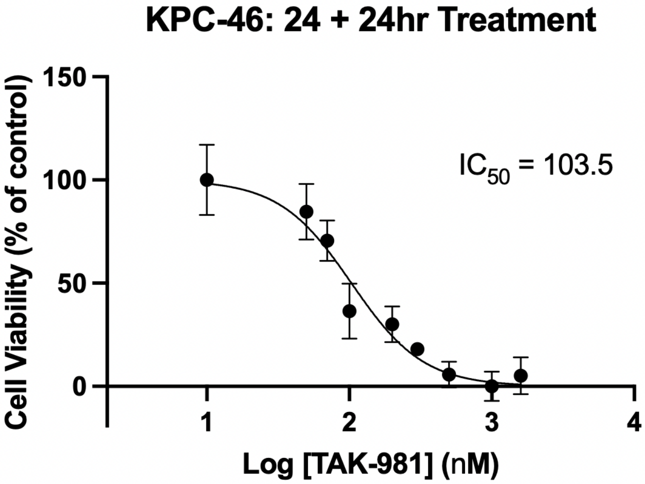

Figure 39. Log [TAK-981](nM) vs cell viability. n = 3

Aldehyde dehydrogenase (ALDH) activity, a characteristic feature in various cancer stem cells, serves as a commonly utilized marker for identifying CSCs (*39*, *40*). The composition of ALDH cells in KPC-46 cells was investigated. This analysis involved analyzing the substrate of ALDH to measure the overall enzymatic activity of ALDH. Following TAK-981 treatment, there was a notable reduction in ALDH$^+$ cells (Fig. 40B). This reduction in the overall enzymatic ALDH activity suggests a potential decrease in CSCs within PDAC cancer cells. This data suggest that the cancer stem cells enzymatic expression level is downregulated by SUMOylation inhibition.

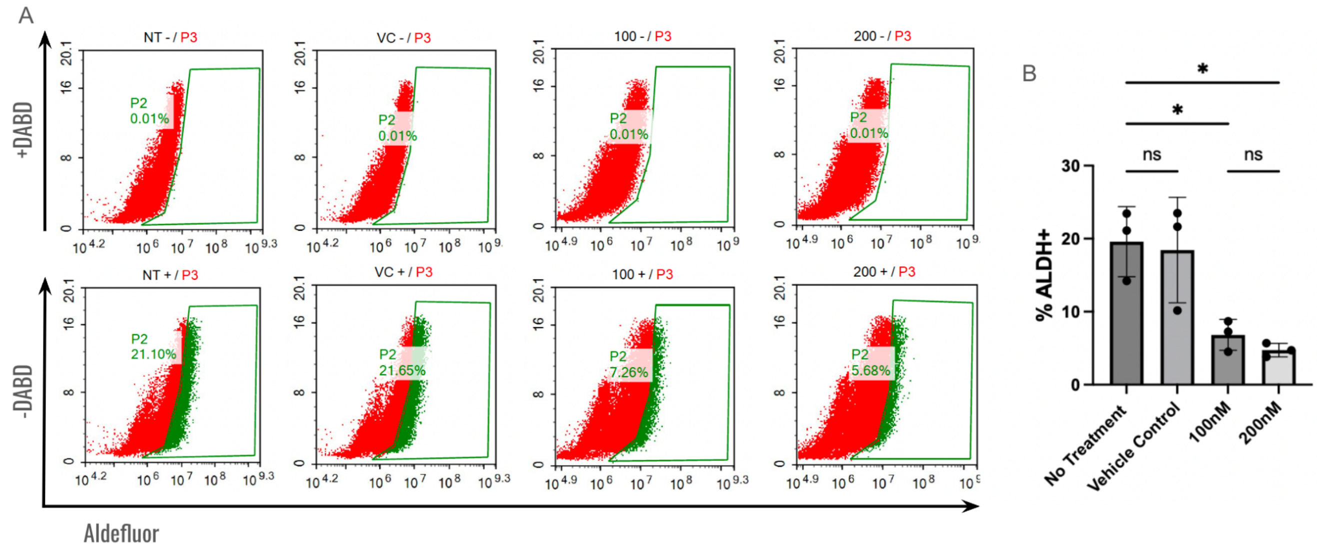

Figure 40: Aldefluor analysis using flow cytometry. A. Gating strategy of ALDH$^+$ cells using ALDH inhibitor: DEAB for negative control. Cells were treated with concentrations of 100 nM and 200 nM for 24 hr. Subsequently, fresh media replacement for another 24 hr was implemented to simulate an environment conducive to CSCs. B. Quantification of the percentage of ALDH$^+$ cells in the KPC-46 cancer cell line in No treatment, vehicle control, 100 nM, and 200 nM TAK-981 treatment. n = 3; * $P < 0.05$.

CHAPTER 4 DISCUSSION

In this study, we have demonstrated that SUMOylation inhibition could be a new strategy for PDAC liver metastasis. Our approach involved engineering the KPC-46 cancer cell line by transducing Zsgreen and Luciferase into the cells that not only established PDAC metastatic model in fully immune competent mice, but also allowed tracking of tumor progression in vivo and ex vivo. This is important due to the formation of diffuse tumors in the liver. Analysis of bioluminescent signals in live mice, as well as examination of fluorescence, phenotype, and liver dissociation, collectively indicate a significant reduction in tumor formation in mice following TAK-981 treatment. We identified potentially multiple effects of SUMOylation inhibition.

To examine metastatic niche formation, qPCR analysis of TAK-981 and vehicle-treated KPC-46 cell lines co-cultured with HSCs from mouse liver showed reduced expression of cytokines that promote tumor growth including CCL20 and IL6. Together with the preliminary analysis of HSC from mice treated with TAK-981, SUMOylation inhibition prevented alteration of HSCs by tumor cells for the establishment of metastatic niche. Additionally, examination of macrophages in the liver revealed increased macrophages in both tumor and non-tumor sites in the vehicle control group, contrasting with similar number of macrophages in the TAK-981 treated and healthy mice. This suggests that SUMOylation inhibition prevented alteration of liver macroenvironments by tumor formation.

For immune effect analysis, PBMCs were collected and NK cells, CD3$^+$ T cells, CD4$^+$ T cells, and CD8$^+$ T cells, memory T cells were further analyzed using flow cytometry. Our findings revealed a statistically significant increase in NK cells, CD3$^+$ T cells, CD8$^+$ T cells, naive CD8$^+$ T cells, and central memory CD8$^+$ T cells and a shift to Tcm within the CD8$^+$ T cells. However, no notable difference was observed in total CD4$^+$ T cells . The observed enhancement in both NK and CD8$^+$ T cells that can possess tumor killing ability, coupled with memory formation, suggests a potential immune-boosting effect after TAK-981 treatment. To delve deeper into this, future investigations will involve performing the same studies on specific immune-cell knockout mice to identify key immune cells influencing SUMOylation inhibition in PDAC. Additionally, assessing the formation of memory cells will involve investigating whether there is an increase in neoantigen-recognizing T cells, the formation of stem-like memory T cells that have garnered recent attention as playing key roles in anti-tumor CD8$^+$ T cell responses, and T cell exhaustion.

In the tumor-specific analysis, we examined the *in vitro* tumor cell proliferation and CSCs inhibition. The analysis of ALDH enzymatic activity revealed a reduction in ALDH$^+$ cells after TAK-981 treatment, suggesting a potential decrease in CSCs formation. To comprehensively validate this hypothesis, subsequent experiments will further validate ALDH$^+$ as a CSC marker in our cell models and examining self-renewal potential using colony formation and limiting dilution assays. Additionally, the use of patient-derived organoids will confirm the relevance of my initial findings to human disease.

To further investigate the molecular mechanisms of SUMOylation inhibition, more inclusive experiments need to be conducted to analyze the SUMO-related proteins and genes.

REFERENCES

1. R. L. Siegel, K. D. Miller, N. S. Wagle, A. Jemal, Cancer statistics, 2023. *CA Cancer J. Clin.* **73**, 17–48 (2023).

2. S. Wang, Y. Zheng, F. Yang, L. Zhu, X.-Q. Zhu, Z.-F. Wang, X.-L. Wu, C.-H. Zhou, J.-Y. Yan, B.-Y. Hu, B. Kong, D.-L. Fu, C. Bruns, Y. Zhao, L.-X. Qin, Q.-Z. Dong, The molecular biology of pancreatic adenocarcinoma: translational challenges and clinical perspectives. *Signal Transduction and Targeted Therapy*. **6** (2021), doi:10.1038/s41392-021-00659-4.

3. Pancreatic Cancer Treatment (PDQ®). *National Cancer Institute* (2023), (available at https://www.cancer.gov/types/pancreatic/hp/pancreatic-treatment-pdq).

4. A. Hoellein, M. Fallahi, S. Schoeffmann, S. Steidle, F. X. Schaub, M. Rudelius, I. Laitinen, L. Nilsson, A. Goga, C. Peschel, J. A. Nilsson, J. L. Cleveland, U. Keller, Myc-induced SUMOylation is a therapeutic vulnerability for B-cell lymphoma. *Blood*. **124**, 2081–2090 (2014).

5. B. Yu, S. Swatkoski, A. Holly, L. C. Lee, V. Giroux, C.-S. Lee, D. Hsu, J. L. Smith, G. Yuen, J. Yue, D. K. Ann, R. M. Simpson, C. J. Creighton, W. D. Figg, M. Gucek, J. Luo, Oncogenesis driven by the Ras/Raf pathway requires the SUMO E2 ligase Ubc9. *Proc. Natl. Acad. Sci. U. S. A.* **112**, E1724 (2015).

6. Y.-J. Li, L. Du, G. Aldana-Masangkay, X. Wang, R. Urak, S. J. Forman, S. T. Rosen, Y. Chen, Regulation of miR-34b/c-targeted gene expression program by SUMOylation. *Nucleic Acids Res.* **46**, 7108–7123 (2018).

7. J. D. Kessler, K. T. Kahle, T. Sun, K. L. Meerbrey, M. R. Schlabach, E. M. Schmitt, S. O. Skinner, Q. Xu, M. Z. Li, Z. C. Hartman, M. Rao, P. Yu, R. Dominguez-Vidana, A. C. Liang, N. L. Solimini, R. J. Bernardi, B. Yu, T. Hsu, I. Golding, J. Luo, C. K. Osborne, C. J. Creighton, S. G. Hilsenbeck, R. Schiff, C. A. Shaw, S. J. Elledge, T. F. Westbrook, A SUMOylation-dependent transcriptional subprogram is required for Myc-driven tumorigenesis. *Science*. **335**, 348–353 (2012).

8. U. Sahin, O. Ferhi, X. Carnec, A. Zamborlini, L. Peres, F. Jollivet, A. Vitaliano-Prunier, Hugues de Thé, V. Lallemand-Breitenbach, Interferon controls SUMO availability via the Lin28 and let-7 axis to impede virus replication. *Nat. Commun.* **5**, 1–8 (2014).

9. S. P. Langston, S. Grossman, D. England, R. Afroze, N. Bence, D. Bowman, N. Bump, R. Chau, B.-C. Chuang, C. Claiborne, L. Cohen, K. Connolly, M. Duffey, N. Durvasula, S. Freeze, Melissa Gallery, K. Galvin, J. Gaulin, R. Gershman, P. Greenspan, J. Grieves, J. Guo, N. Gulavita, S. Hailu, X. He, K. Hoar, Y. Hu, Z. Hu, M. Ito, M.-S. Kim, S. W. Lane, D. Lok, A. Lublinsky, W. Mallender, C. McIntyre, J. Minissale, H. Mizutani, M. Mizutani, N. Molchinova, K. Ono, A. Patil, M. Qian, J. Riceberg, V. Shindi, M. D. Sintchak, K. Song, T. Soucy, Y. Wang, H. Xu, X. Yang, A. Zawadzka, J. Zhang, S. M. Pulukuri, Discovery of TAK-981, a First-in-Class Inhibitor of SUMO-Activating Enzyme for the Treatment of Cancer. *J. Med. Chem.* (2021), doi:10.1021/acs.jmedchem.0c01491.

10. X.-D. Zhang, J. Goeres, H. Zhang, T. J. Yen, A. C. G. Porter, M. J. Matunis, SUMO-2/3 modification and binding regulate the association of CENP-E with kinetochores and progression through mitosis. *Mol. Cell*. **29**, 729–741 (2008).

11. A. B. Celen, U. Sahin, Sumoylation on its 25th anniversary: mechanisms, pathology, and emerging concepts. *FEBS J.* **287**, 3110–3140 (2020).

12. J. R. Gareau, C. D. Lima, The SUMO pathway: emerging mechanisms that shape specificity, conjugation and recognition. *Nat. Rev. Mol. Cell Biol.* **11**, 861–871 (2010).

13. J. E. Brownell, M. D. Sintchak, J. M. Gavin, H. Liao, F. J. Bruzzese, N. J. Bump, T. A. Soucy, M. A. Milhollen, X. Yang, A. L. Burkhardt, J. Ma, H.-K. Loke, T. Lingaraj, D. Wu, K. B. Hamman, J. J. Spelman, C. A. Cullis, S. P. Langston, S. Vyskocil, T. B. Sells, W. D. Mallender, I. Visiers, P. Li, C. F. Claiborne, M. Rolfe, J. B. Bolen, L. R. Dick, Substrate-assisted inhibition of ubiquitin-like protein-activating enzymes: The NEDD8 E1 inhibitor MLN4924 forms a NEDD8-AMP mimetic in situ. *Mol. Cell*. **37**, 102–111 (2010).

14. J. J. Chen, C. A. Tsu, J. M. Gavin, M. A. Milhollen, F. J. Bruzzese, W. D. Mallender, M. D. Sintchak, N. J. Bump, X. Yang, J. Ma, H.-K. Loke, Q. Xu, P. Li, N. F. Bence, J. E. Brownell, L. R. Dick, Mechanistic studies of substrate-assisted inhibition of ubiquitin-activating enzyme by adenosine sulfamate analogues. *J. Biol. Chem.* **286**, 40867–40877 (2011).

15. TAK-981 - Chemietek, (available at https://www.chemietek.com/tak-981-details.aspx).

16. A. Biederstädt, Z. Hassan, C. Schneeweis, M. Schick, L. Schneider, A. Muckenhuber, Y. Hong, G. Siegers, L. Nilsson, M. Wirth, Z. Dantes, K. Steiger, K. Schunck, S. Langston, H.-P. Lenhof, A. Coluccio, F. Orben, J. Slawska, A. Scherger, D. Saur, S. Müller, R. Rad, W. Weichert, J. Nilsson, M. Reichert, G. Schneider, U. Keller, Original research: SUMO pathway inhibition targets an aggressive pancreatic cancer subtype. *Gut*. **69**, 1472 (2020).

17. Expression of SAE1 in pancreatic cancer - The Human Protein Atlas, (available at https://www.proteinatlas.org/ENSG00000142230-SAE1/pathology/pancreatic+cancer#ihc).

18. Expression of SUMO1 in pancreatic cancer - The Human Protein Atlas, (available at https://www.proteinatlas.org/ENSG00000116030-SUMO1/pathology/pancreatic+cancer#ihc).

19. Expression of SUMO2 in pancreatic cancer - The Human Protein Atlas, (available at https://www.proteinatlas.org/ENSG00000188612-SUMO2/pathology/pancreatic+cancer#ihc).

20. Expression of SUMO3 in pancreatic cancer - The Human Protein Atlas, (available at https://www.proteinatlas.org/ENSG00000184900-SUMO3/pathology/pancreatic+cancer#ihc).

21. Expression of UBA2 in pancreatic cancer - The Human Protein Atlas, (available at https://www.proteinatlas.org/ENSG00000126261-UBA2/pathology/pancreatic+cancer#ihc).

22. Expression of UBE2I in pancreatic cancer - The Human Protein Atlas, (available at https://www.proteinatlas.org/ENSG00000103275-UBE2I/pathology/pancreatic+cancer#ihc).

23. L. Li, M. Duan, W. Chen, A. Jiang, X. Li, J. Yang, Z. Li, The spleen in liver cirrhosis: revisiting an old enemy with novel targets. *J. Transl. Med.* **15**, 1–10 (2017).

24. H. S. Jacob, Overview of the Spleen. *Merck Manuals Consumer Version*, (available at https://www.merckmanuals.com/home/blood-disorders/spleen-disorders/overview-of-the-spleen).

25. K. C. Soares, K. Foley, K. Olino, A. Leubner, S. C. Mayo, A. Jain, E. Jaffee, R. D. Schulick, K. Yoshimura, B. Edil, L. Zheng, A Preclinical Murine Model of Hepatic Metastases. *J. Vis. Exp.* (2014), doi:10.3791/51677.

26. A third-generation lentivirus vector with a conditional packaging system. Dull T, Zufferey R, Kelly M, Mandel RJ, Nguyen M, Trono D, Naldini L. J Virol. 1998 Nov . 72(11):8463-71. PubMed 9765382

27. A third-generation lentivirus vector with a conditional packaging system. Dull T, Zufferey R, Kelly M, Mandel RJ, Nguyen M, Trono D, Naldini L. J Virol. 1998 Nov . 72(11):8463-71. PubMed 9765382

28. J. J. Pitt, Principles and applications of liquid chromatography-mass spectrometry in clinical biochemistry. *Clin. Biochem. Rev.* **30**, 19–34 (2009).

29. Nuclear Magnetic Resonance Spectroscopy, , doi:10.1016/B978-0-12-821280-6.00008-8.

30. S. Bhal, The Basics of Interpreting a Proton (1H) NMR Spectrum. *ACD/Labs* (2021), (available at https://www.acdlabs.com/blog/the-basics-of-interpreting-a-proton-nmr-spectrum/).

31. H. Peinado, H. Zhang, I. R. Matei, B. Costa-Silva, A. Hoshino, G. Rodrigues, B. Psaila, R. N. Kaplan, J. F. Bromberg, Y. Kang, M. J. Bissell, T. R. Cox, A. J. Giaccia, J. T. Erler, S. Hiratsuka, C. M. Ghajar, D. Lyden, Pre-metastatic niches: organ-specific homes for metastases. *Nat. Rev. Cancer*. **17**, 302–317 (2017).

32. J. Elegheert, E. Behiels, B. Bishop, S. Scott, R. E. Woolley, S. C. Griffiths, E. F. X. Byrne, V. T. Chang, D. I. Stuart, E. Yvonne Jones, C. Siebold, A. Radu Aricescu, Lentiviral transduction of mammalian cells for fast, scalable and high-level production of soluble and membrane proteins. *Nat. Protoc.* **13**, 2991 (2018).

33. Addgene: pHIV-Luc-ZsGreen, (available at https://www.addgene.org/39196/).

34. R. T. Sadikot, Bioluminescence imaging. *Proc. Am. Thorac. Soc.* **2**, 537–540 (2005).

35. J. S. Marshall, R. Warrington, W. Watson, H. L. Kim, An introduction to immunology and immunopathology. *Allergy Asthma Clin. Immunol.* **14**, 1–10 (2018).

36. T. Gebhardt, S. L. Park, I. A. Parish, Stem-like exhausted and memory CD8+ T cells in cancer. *Nat. Rev. Cancer*. **23**, 780–798 (2023).

37. Y. Zhu, J. M. Herndon, D. K. Sojka, K.-W. Kim, B. L. Knolhoff, C. Zuo, D. R. Cullinan, J. Luo, A. R. Bearden, K. J. Lavine, W. M. Yokoyama, W. G. Hawkins, R. C. Fields, G. J. Randolph, D. G. DeNardo, Tissue-resident macrophages in pancreatic ductal adenocarcinoma originate from embryonic hematopoiesis and promote tumor progression. *Immunity*. **47**, 323-338.e6 (2017).

38. H.-M. Zhou, J.-G. Zhang, X. Zhang, Q. Li, Targeting cancer stem cells for reversing therapy resistance: mechanism, signaling, and prospective agents. *Signal Transduction and Targeted Therapy*. **6**, 1–17 (2021).

39. D. W. Clark, K. Palle, Aldehyde dehydrogenases in cancer stem cells: potential as therapeutic targets. *Annals of Translational Medicine*. **4** (2016), doi:10.21037/atm.2016.11.82.

40. H. Tomita, K. Tanaka, T. Tanaka, A. Hara, Aldehyde dehydrogenase 1A1 in stem cells and cancer. *Oncotarget*. **7**, 11018–11032 (2016).